Author/s:
Selig, EE;Lynn, RJ;Zlatic, CO;Mok, Y-F;Ecroyd, H;Gooley, PR;Griffin, MDW

Title:
The Monomeric α-Crystallin Domain of the Small Heat-shock Proteins αB-crystallin and Hsp27 Binds Amyloid Fibril Ends

Date:
2022-08-30

Citation:
Selig, E. E., Lynn, R. J., Zlatic, C. O., Mok, Y. -F., Ecroyd, H., Gooley, P. R. & Griffin, M. D. W. (2022). The Monomeric α-Crystallin Domain of the Small Heat-shock Proteins αB-crystallin and Hsp27 Binds Amyloid Fibril Ends. JOURNAL OF MOLECULAR BIOLOGY, 434 (16), https://doi.org/10.1016/j.jmb.2022.167711.

The monomeric α-crystallin domain of the small heat-shock proteins αB-crystallin and Hsp27 binds amyloid fibril ends.

Emily E. Selig[a], Roberta J. Lynn[a], Courtney O. Zlatic[a], Yee-Foong Mok[a], Heath Ecroyd[b,c], Paul R. Gooley[a#] and Michael D.W. Griffin[a#]*

[a] Department of Biochemistry and Pharmacology, University of Melbourne, Parkville, Victoria 3010, Australia and Bio21 Molecular Science and Biotechnology Institute, University of Melbourne, Parkville, Victoria 3010, Australia.

[b] Molecular Horizons and School of Chemistry and Molecular Bioscience, University of Wollongong, Wollongong, NSW 2522, Australia

[c] Illawarra Health and Medical Research Institute, Wollongong, NSW 2522, Australia

[#] These authors contributed equally

* To whom correspondence should be addressed: Department of Biochemistry and Pharmacology, Bio21 Molecular Science and Biotechnology Institute, University of Melbourne, 30 Flemington Road, Parkville, Victoria 3010, Australia. Tel.: 61-3-9035-4233; Fax: 61-3-9348-1421; e-mail: mgriffin@unimelb.edu.au

selige@uthscsa.edu, roberta.j.lynn@gmail.com, courtney.zlatic@unimelb.edu.au, ymok@unimelb.edu.au, heathe@uow.edu.au, prg@unimelb.edu.au, mgriffin@unimelb.edu.au

– Abstract –

Small heat-shock proteins (sHSPs) are ubiquitously expressed molecular chaperones present in all kingdoms of life that inhibit protein misfolding and aggregation. Despite their importance in proteostasis, the structure-function relationships of sHSPs remain elusive. Human sHSPs are characterised by a central, highly conserved α-crystallin domain (ACD) and variable-length N- and C-terminal regions. The ACD forms antiparallel homodimers via an extended β-strand, creating a shared β-sheet at the dimer interface. The N- and C-terminal regions mediate formation of higher order oligomers that are thought to act as storage forms for chaperone-active dimers. We investigated the interactions of the ACD of two human sHSPs, αB-crystallin (αB-C) and Hsp27, with apolipoprotein C-II amyloid fibrils using analytical ultracentrifugation and nuclear magnetic resonance spectroscopy. The ACD was found to interact transiently with amyloid fibrils to inhibit fibril elongation and naturally occurring fibril end-to-end joining. This interaction was sensitive to the concentration of fibril ends indicating a 'fibril-capping' interaction. Furthermore, resonances arising from the ACD monomer were attenuated to a greater extent than those of the ACD dimer in the presence of fibrils, suggesting that the monomer may bind fibrils. This hypothesis was supported by mutagenesis studies in which disulfide cross-linked ACD dimers formed by both αB-C and Hsp27 were less effective at inhibiting amyloid fibril elongation and fibril end-to-end joining than ACD constructs lacking disulfide cross-linking. Our results indicate that sHSP monomers inhibit amyloid fibril elongation, highlighting the importance of the dynamic oligomeric nature of sHSPs for client binding.

– Keywords –

Molecular chaperone, nuclear magnetic resonance, analytical ultracentrifugation, apolipoprotein C-II

– Introduction –

Small heat-shock proteins (sHSPs) are an evolutionarily conserved class of molecular chaperones that are present in all kingdoms of life. sHSPs are ATP-independent chaperones that function in tandem with ATP-dependent chaperones to fold and/or refold a vast array of clients and also assist in targeting misfolded proteins for proteolytic degradation [1,2]. sHSPs therefore play major roles in proteostasis. Mutations in sHSPs are associated with neuropathies [3], myopathies [4] and cataracts.

The monomeric mass of sHSPs ranges from 15-40 kDa and some mammalian sHSPs assemble into polydisperse oligomers that can range from dimers to 40- or 50-mers [5,6]. The sHSP monomer comprises a central, highly conserved, ~90-residue domain termed the α-crystallin domain (ACD) that is flanked by poorly conserved N- and C-terminal regions (NTR and CTR, respectively). Much of the structural information regarding mammalian sHSPs has come from high-resolution structures of monodisperse plant or prokaryotic sHSPs [7,8] or structures of the isolated ACD of several human sHSPs [9–12]. Of the ten human sHSPs (HSPB1-10) the most widely studied is αB-crystallin (αB-C, HspB5). Models of a 24-mer of αB-C have been constructed using a combination of solid-state nuclear magnetic resonance (NMR) spectroscopy, small-angle X-ray scattering, electron microscopy (EM) and ion-mobility mass spectrometry [13–15]. Crystal structures of the isolated ACD of several human sHSPs, including αB-C, reveal that this domain adopts an Ig-like fold with six or seven antiparallel β-strands assembled into two β-sheets. The β-strands are numbered β2 (which is not present in all structures), β3, β4, β5, β6+7, β8 and β9 [9,11,12]. In almost all structures solved to date, the ACD forms a homodimer, with the elongated β6+7 strand forming an antiparallel interface between the two subunits. A peptide corresponding to a conserved IXI/V motif in the CTR binds to a hydrophobic groove formed between the outward-facing β4 and β8 strands of the ACD [11,12]. The assembly of αB-C oligomers is thought to occur hierarchically; two ACDs interact via the β6+7 strand to form a dimer, their CTRs dock to the ACDs of nearby dimers via the conserved IXI/V motif to form small oligomers and the NTR contributes to a higher order oligomeric assembly [16].

Attempts to unambiguously identify the client-binding sites of sHSPs such as αB-C and Hsp27 (HSPB1) has proven difficult despite extensive research efforts over the past two decades. This

has led to the proposal that sHSPs may interact with different clients via distinct binding sites that are not likely to be confined to any one of the three sHSP regions, the NTR, ACD and CTR [17,18]. Efforts to delineate the interactions between sHSPs and various client proteins have typically focused on the early stages of amyloid formation, prior to the formation of large aggregates. In the case of amyloidogenic client proteins, sHSPs including αB-C have often been found to interact with their clients via extremely transient interactions that are difficult to detect [19]. Weak interactions between the isolated ACD of αB-C or Hsp27 with several client proteins prior to aggregation have been identified using solution NMR [20–23]. In contrast to these studies, the interaction of sHSPs with client proteins that are already aggregated has been shown to be relatively stable, and Hsp27 and αB-C have been identified in senile plaques and Lewy bodies [24–26]. αB-C and Hsp27 also stably colocalise with amyloid fibrils formed *in vitro* [27–32]. The function of this binding has been proposed to inhibit the nucleation-dependent polymerization of fibrils [28,29], stabilize fibrils against fragmentation [30], sequester fibrils and oligomers into larger aggregates [30,32,33], and reduce the cytotoxicity of fibrils [31,34].

In this work, we focused our attention on the isolated ACD of αB-C, which exhibits chaperone activity against amyloid formation by κ-casein [12], $A\beta_{1-42}$ [12], $A\beta_{1-40}$ [20], α-synuclein [19,21] and apolipoprotein C-II (apoC-II) [32]. However, it has been speculated that the ACD exerts these effects via interactions with the early intermediates of amyloid formation. Our aims were to investigate whether the ACD of αB-C can interact with amyloid fibrils as part of its chaperone function. We demonstrate that αB-C ACD inhibited apoC-II fibril elongation and naturally occurring end-to-end joining via a transient interaction with the ends of the fibrils. Conditions favouring dissociation of αB-C ACD dimers to monomers enhanced the association of the ACD with apoC-II fibrils, suggesting that the monomer contributes to this observed chaperone activity of αB-C ACD. Supporting this hypothesis, disulfide crosslinking at the dimer interface impaired the chaperone activity of both αB-C ACD and the closely related Hsp27 (HspB1) ACD. Importantly, disulfide crosslinking at the dimer interface also impaired the chaperone activity of the full-length WT proteins, demonstrating that our findings regarding the ACD are also relevant in the context of the physiologically relevant protein forms.

– Results –

αB-C ACD inhibits apoC-II fibril elongation and fibril end-to-end joining

We have previously shown that truncated constructs of the sHSPs αB-C and Hsp27 inhibit apoC-II fibril formation [32]. ThT fluorescence assays indicate that both WT αB-C and αB-C ACD reduce the rate of apoC-II fibril formation (Fig. 1A) [32]. Nevertheless, fibril formation still occurs in the presence of both constructs at the concentrations we tested. Therefore, we sought to determine whether the presence of the sHSPs reduces the lengths of the fibrils formed. To do this, we used both SV-AUC (Fig. 1B), which is a well-established technique for determining apoC-II fibril size distributions [35–38], and transmission electron microscopy (TEM) (Fig. 1C-E). AUC demonstrated that the presence of both αB-C constructs resulted in shorter fibrils being formed over the 168-hour incubation period and TEM showed that the fibrils were morphologically similar to those formed in the absence of αB-C. In particular, the size distribution of apoC-II fibrils formed in the presence of αB-C ACD was considerably left-shifted relative to apoC-II fibrils formed alone, indicating shorter fibrils (Fig. 1B). Additionally, WT αB-C and αB-C ACD were both found to inhibit apoC-II fibril elongation when these proteins were added at various timepoints during fibril formation rather than at the initiation of fibril formation (Fig. S1). Based on these findings we hypothesized that the ACD may interact with fibril ends to inhibit fibril elongation.

To further investigate the inhibition of apoC-II fibril formation by αB-C, we made use of an interesting property of apoC-II fibrils: Upon fragmenting apoC-II fibrils by sonication, the fibrils undergo end-to-end joining to re-establish their original size distributions [35]. Here we fragmented apoC-II fibrils by ultrasonication and immediately added αB-C ACD at various sub-stoichiometric concentrations. The fibril size distributions were analysed by AUC immediately (Fig. 1F), or after 72 hours (Fig. 1G). The total duration of the AUC experiment is approximately 7 hours, therefore the data in Fig. 1F represent an early timepoint after fragmentation but not a true 0-hour timepoint. It is likely that fragmented fibrils incubated alone undergo substantial end-to-end joining before the AUC experiment begins, causing the differences seen at 0 hours. Supporting this is our observation that if the experiment was performed at 10 °C, where fibril end-to-end joining is slower, the fibril size distribution is left-shifted relative to that obtained at 20 °C (Fig. S2A). Furthermore, fitting only a subset of early SV-AUC scans reveals that the size distribution increases throughout the duration of the experiment (Fig. S2B). At the early timepoint, fibrils

incubated with equal to or greater than a 1:70 molar ratio of αB-C ACD:apoC-II were substantially shorter than those incubated alone, indicating that fibril end-to-end joining was inhibited (Fig. 1F and G). Molar ratios of 1:70, 1:18 and 1:4 all resulted in similar fibril size distributions, indicating saturation of the effect of αB-C ACD on rejoining at molar ratios above 1:70. At a molar ratio of 1:1120, the effect of αB-C ACD on apoC-II fibril end-to-end joining was noticeably reduced. Over the 72-hour incubation at room temperature, concentration-dependence of the effect of αB-C ACD on apoC-II end-to-end joining is more readily observed.

WT αB-C displays some ability to inhibit fibril end-to-end joining (Fig. S3), however WT αB-C also forms a stable interaction with the fibrils over time and induces fibril tangling, increasing their mass and apparent sedimentation coefficient [32]. Fibril binding and fibril tangling induced by WT αB-C has a right-shifting effect on the fibril size distribution, confounding any quantitative analysis and thus we have focused on the ACD of αB-C, which does not stably interact with apoC-II fibrils [32]. The non-chaperone proteins BSA, ovalbumin and lysozyme displayed no effect on apoC-II fibril rejoining (Fig. S4).

αB-C ACD interacts transiently with apoC-II fibril ends

Previously we determined that αB-C ACD does not stably associate with apoC-II fibrils at levels detectable by SDS-PAGE [32]. We were also unable to pull-down apoC-II fibrils using nickel NTA resin in the presence of 6x His-tagged αB-C ACD (Fig. S5), which likely indicates that any interaction between αB-C ACD and apoC-II fibrils is transient in nature. To further interrogate a transient interaction between αB-C ACD and apoC-II amyloid fibrils we used solution NMR. The addition of apoC-II fibrils to samples containing ^{15}N-labelled αB-C ACD was consistently found to induce modest loss of signal intensity across all peaks in ^{15}N-HSQC spectra (Fig. S6). This may be indicative of an interaction between αB-C ACD and the fibrils because transient fibril binding would reduce the tumbling rate of αB-C ACD leading to a loss of signal intensity.

Given our prior observations that αB-C ACD inhibited apoC-II fibril end-to-end joining at sub-stoichiometric concentrations (Fig. 1F-G), we hypothesized that the extent of signal intensity loss in ^{15}N-HSQC spectra may be dependent on the concentration of free fibril ends, not simply apoC-II concentration. To test this hypothesis, we recorded ^{15}N-HSQC spectra of αB-C ACD (50 μM)

in the presence of a high concentration of fibrils (10 mg/mL, or 1120 μM apoC-II) prior to sonication ("long fibrils") and after sonication ("short fibrils"). We used a wormlike chain model relating the sedimentation coefficient of apoC-II fibrils to their molecular weight (MW) to estimate the average fibril MW and to approximate the concentration of fibril ends for the long fibrils and the short fibrils. Long fibrils exhibit a size distribution with a weight-average sedimentation coefficient of ~130 S (Fig. 1B). This corresponds to a weight-average fibril mass of ~31 MDa with approximately 3500 monomeric subunits of apoC-II per average fibril. At a protein concentration of 1120 μM, we approximate the concentration of free fibril ends for long fibrils as 0.6 μM. After sonication, the weight-average sedimentation coefficient of the fibrils is reduced to ~26 S (Fig. 1F), corresponding to a MW of 830 kDa, ~90 monomeric subunits of apoC-II per weight-average fibril and a concentration of fibril ends for short fibrils of approximately 24 μM. Therefore, at 1120 μM apoC-II, the concentration of free fibril ends can be altered by at least one order of magnitude by this sonication method in order to test whether αB-C ACD displays a preference for binding to fibril ends.

When ^{15}N-labelled αB-C ACD was incubated in the presence of 1120 μM apoC-II as long fibrils, the signal intensity of peaks corresponding to αB-C ACD was reduced relative to αB-C ACD incubated alone (Fig. 2A-B), however no large peak shifts were observed. To rule out non-specific effects that could be induced by an increase in sample viscosity due to the relatively high concentration of apoC-II used, we also recorded a ^{15}N-HSQC spectrum of αB-C ACD incubated in the presence of an identical mass of BSA (10 mg/mL, 150 μM) (Fig. S7A, Fig. 2D). Unlike the sample containing fibrils, no significant peak broadening was observed, indicating that αB-C ACD does not interact with BSA, and that small changes in sample viscosity arising from the high protein concentration does not cause a loss of signal intensity.

Following sonication to generate short fibrils of apoC-II, the ^{15}N-HSQC spectra of αB-C ACD was broadened to such an extent as to be almost entirely undetectable, except for peaks corresponding to highly dynamic regions of αB-C ACD such as glutamine and asparagine side chains and residues near the C-terminus (V152, S153, Fig. 2A, C). To confirm that the process of sonication did not affect the signal intensity of peaks corresponding to αB-C ACD, a spectrum was recorded on a separate sample of αB-C ACD alone after sonication (Fig. 2E, Fig. S7B). Intensity ratios (I/I_0)

were calculated for all assigned peaks across the spectra for all samples relative to αB-C ACD alone (Fig. 2B-E). For each sample, the mean I/I_0 ratio (relative to αB-C ACD alone prior to sonication) and the standard deviation (SD) observed across all residues were also computed to enable comparisons between samples. Sonication alone or the presence of BSA did not affect the signal intensity of αB-C ACD, with I/I_0 ratios of 0.96 ± 0.08 and 1.04 ± 0.06 for these samples, respectively (Fig. 2D and E, respectively). Incubation with long apoC-II fibrils resulted in I/I_0 ratios of 0.31 ± 0.07, indicating an interaction between the fibrils and αB-C ACD (Fig. 2B). However, after fragmentation of the fibrils, the I/I_0 ratios were further reduced to 0.07 ± 0.06 (Fig. 2C). The differential I/I_0 ratios observed for the same sample before and after fibril fragmentation indicates that a larger population of αB-C ACD interacts with the shorter fibrils relative to the longer fibrils. Therefore, αB-C ACD exhibits a preference for binding fibrils ends as opposed to the surface of the fibril. However, these data do not rule out an additional, low-affinity interaction of αB-C ACD with the fibril surface.

AUC and NMR reveal the equilibrium between αB-C ACD monomers and dimers

Close inspection of the spectra in Fig. 2A revealed the presence of weak peaks that have not been assigned. These are evident in the asparagine/glutamine side-chain region as well as in the centre of the spectrum, between 7.5 and 8.5 ppm where we may expect resonances from a region of disorder to occur (Fig. 2A). We consistently observed the same resonances in ^{15}N-HSQC spectra collected on multiple different preparations of αB-C ACD (Fig. S6A), indicating that these were not due to contaminants or protein degradation. Furthermore, close inspection of previously published spectra of similar constructs of αB-C ACD also revealed weak peaks with comparable chemical shifts [21,39,40]. This observation indicated that these unassigned peaks are likely to arise from an alternative conformation of αB-C ACD, possibly a monomeric species that contains dynamic regions. These weak resonances became more pronounced at lower pH, in agreement with other published data [39,40]. Notably, previously reported isothermal titration calorimetry measurements also suggest that a reduction in pH increases the population of αB-C ACD monomers by increasing the monomer-dimer dissociation constant (K_D) [39]. We therefore hypothesized that the weak peaks observed in our spectra and in previously published spectra of similar constructs could arise from αB-C ACD monomers. This hypothesis is also supported by recently published NMR data for the Hsp27 ACD across a pH range of 7.0 to 4.5 [41]. Spectra

acquired at low concentrations (20 μM), low pH (4.5) and/or high pressure (≤ 1.6 kbar) enabled the Hsp27 ACD monomer to be distinguished from the dimer using NMR [41]. To further investigate the monomer-dimer equilibrium of αB-C ACD we utilised AUC to characterise dimer dissociation at various protein concentrations and across the pH range 7.4 to 6.0. A reduction in pH from 7.4 to 6.0 shifted the weight-average sedimentation coefficient of αB-C ACD from 1.61 S to 1.36 S, consistent with an increase in the proportion of monomer (Fig. 3A, B). Mutation of residue E117 at the centre of the αB-C ACD dimer interface to a cysteine residue, which mimics a naturally occurring cysteine residue in the ACD of Hsp27, enables the formation of a disulfide cross-linked αB-C ACD dimer [12]. This mutation resulted in a small but consistent increase in the weight-average sedimentation coefficient of αB-C ACD to 1.87 S, suggesting that in the absence of disulfide cross-linking, the αB-C ACD dimer dissociates to monomers even at neutral pH. In contrast to the WT αB-C ACD, the weight-average sedimentation coefficient of the E117C αB-C ACD was not altered by a reduction in pH (Fig. 3B). However, the addition of TCEP at both pH 7.4 and pH 6.0 reduced the weight-average sedimentation coefficient to 1.65 S and 1.48 S, respectively. A bimodal sedimentation coefficient distribution was obtained for WT αB-C ACD at pH 7.4 in the presence of TCEP, indicating that this construct significantly populates the monomeric form even at pH 7.4 (Fig. 3B). Overall, these findings provide further evidence that the WT αB-C ACD construct exists in a monomer-dimer equilibrium at pH 7.4, and that the equilibrium is shifted towards the monomer by reducing the pH or towards the dimer by disulfide cross-linking at both pH 6.0 and pH 7.4.

As αB-C ACD populated both the monomeric and dimeric form under the conditions we used for our chaperone activity assays, we sought to determine whether the monomeric form contributed to the observed chaperone activity. The dimer dissociation constant of αB-C ACD has previously been reported at approximately 2 μM using native mass-spectrometry and ITC at neutral pH [12,39], a protein concentration likely to be too low for observation on most available NMR spectrometers. Therefore, we investigated the monomer-dimer equilibrium at pH 6.0 using both AUC and NMR. At this pH, AUC revealed that the αB-C ACD monomer is the predominant species at concentrations less than or equal to 50 μM (Fig. 3C). At concentrations above 50 μM, the dimer becomes predominant. Weight average sedimentation coefficients were calculated from the distributions in Fig. 3C and fitted to a monomer-dimer self-association model, yielding a dimer

dissociation constant (K_D) estimate of approximately 61 μM (Fig. 3D). We therefore collected ^{15}N-HSQC spectra at concentrations of 25 μM (Fig. 3E), 50 μM, 100 μM and 200 μM (Fig. S8) at both pH 7.4 and pH 6.0. At a concentration of 25 μM and at pH 6.0, AUC indicates that the monomeric species should predominate. At this concentration, a large number of resonances showed significant pH-dependent chemical shifts and others were broadened beyond detection at pH 6.0. Some peaks could be identified based on previously published spectra [39], and by carefully comparing spectra across the concentration series. As expected on the basis of a concentration-dependent monomer-dimer equilibrium, a larger number of residues were unidentifiable in the spectra obtained at 25 μM, pH 6.0 relative to that obtained at 200 μM, pH 6.0. The only residues that were unidentifiable at 200 μM, pH 6.0 were histidine residues (H84, H101, H111), a stretch of six residues at the dimer interface (F113-F118) or peaks that could not be confidently assigned due to signal overlap. These changes likely reflect the protonation of the histidine residues within the protein as well as chemical exchange occurring at the dimer interface. We calculated chemical shift perturbations (CSPs) for resonances that could be identified at both pH 7.4 and pH 6.0 at all four concentrations (Fig. 3F-I). The residues that could no longer be identified at pH 6 were consistently clustered to two main regions: the β3 strand + loop 3-4, and the C-terminal portion of the β5 strand through the entire β6+7 strand and the N-terminal portion of loop 7-8. These two regions were mapped onto the crystal structure of the dimer of αB-C ACD and include all the histidine residues (Fig. 3J). In addition to these changes, many new peaks appear in the spectra obtained at pH 6.0 and mostly within the region 7.5 to 8.5 ppm. Importantly, these peaks are not due to contaminants or protein degradation as we have collected spectra at a range of different pHs on several different preparations of αB-C ACD and have also observed that the spectral changes that occur upon reducing the pH from 7.4 to 6.0 are reversed by increasing the pH back to 7.4 (Fig. S10). Due to the low signal/noise ratio at the concentrations required for a predominant monomer population we were not able to assign these peaks. Nevertheless, these new resonances, which are more distinct at pH 6.0 than 7.4, are consistent with the formation of a monomer, supporting our AUC data. The formation of the monomer arises from a change in conformation occurring at the dimer interface.

The interaction of αB-C ACD with apoC-II fibrils is enhanced under acidic conditions

We used NMR to examine whether a reduction in pH, which perturbs the equilibrium between

αB-C ACD monomers and dimers, affects the interaction of αB-C ACD with apoC-II amyloid fibrils. Similar to our previous assays, to minimise pH effects on the kinetics of apoC-II fibril formation, fibrils were formed at pH 7.4 before being pelleted and resuspended in a buffer containing ^{15}N-labelled αB-C ACD at pH 7.4 or at pH 6.0. Reference spectra of αB-C ACD alone were also collected in both buffers. For this experiment, we altered the ratio of apoC-II:αB-C ACD because we observed that the extent of signal intensity loss is dependent on the concentration of apoC-II fibrils, whether the fibrils are fragmented, and the concentration of αB-C ACD. Here, a higher signal to noise ratio was desirable to discern any differences in the extent of broadening between the samples at the two different pHs. As expected, at 50 μM αB-C ACD and 56 μM fragmented apoC-II fibrils, a loss of signal intensity was observed for peaks corresponding to αB-C ACD in the ^{15}N-HSQC (Fig. 4A) with no substantial changes in peak position observed. At pH 6.0, there was a clear increase in the extent of signal intensity loss across the entire spectrum in the presence of fibrils relative to in the absence of fibrils (Fig. 4B). This loss of signal intensity provides evidence for an interaction between monomeric αB-C ACD and apoC-II fibrils under these conditions.

Signal intensity ratios (I/I_0) were calculated for each backbone amide resonance at both pH 7.4 and 6.0 (Fig. 4C-E). At pH 7.4, I/I_0 in the presence of fibrils relative to in the absence of fibrils, averaged across all backbone amides, was 0.82 ± 0.03 (Fig. 4C). At pH 6.0, more than 50 additional peaks can be observed in the reference spectra and the signal intensity was calculated for both the assigned peaks and these new, unassigned peaks (Fig. 4D-E). The average I/I_0 at pH 6.0 in the presence of fibrils relative to in the absence of fibrils was 0.52 ± 0.15 and 0.43 ± 0.11 for the assigned and unassigned peaks, respectively. Overall, this experiment indicates that a larger proportion of αB-C ACD interacts with apoC-II fibrils under conditions where the population of monomer is increased by a reduction in pH.

We also observed that at pH 7.4, some of the additional unassigned peaks were visible (Fig. 4A). Assuming a dimer dissociation constant of 2 μM at pH 7.4 [12,39], the concentration of monomers is expected to be ~12.5 μM in these experiments. Long acquisition times (~6 hours) substantially improved the signal to noise ratio and our ability to resolve these weak peaks.

Given that peaks corresponding to αB-C ACD monomer were also observed at pH 7.4, we hypothesized that if the αB-C ACD monomer interacts with apoC-II fibrils with a higher affinity than the dimer, the unassigned peaks may be broadened to a greater extent than the assigned peaks in the presence of fibrils. We tested this using 100 μM αB-C ACD in the presence of 1120 μM apoC-II short fibrils and using a higher magnetic field strength to improve signal to noise (800 MHz). Fourteen additional peaks were observable using these conditions (Fig. 5A). A qualitative comparison of the spectra obtained in the absence versus the presence of short fibrils indicates that the peaks that are most affected by the fibrils are the unassigned peaks. The signal intensity ratio (I/I_0) observed for the assigned peaks across the entire spectra was 0.49 ± 0.08 (Fig. 5B). However, the extent of signal intensity loss observed for the unassigned peaks was considerably greater, with an average I/I_0 of 0.10 ± 0.15 (Fig. 5C). We have observed this same trend of increased peak broadening for the unassigned peaks relative to the assigned peaks across multiple similar experiments acquired at different molar ratios of apoC-II:αB-C ACD and in buffers of differing pH (Figs. S6 and S11 – S13). We also observed that unassigned peaks corresponding to αB-C ACD were broadened to a greater extent than assigned peaks when ^{15}N αB-C ACD was mixed with α-synuclein fibrils (Fig. S14), indicating that the monomeric form of αB-C ACD may also interact with fibrils formed by other precursor proteins.

Inhibition of fibril elongation and end-to-end rejoining is also mediated by Hsp27

Previously we demonstrated that various constructs of Hsp27 inhibit apoC-II fibril formation [32]. As mentioned above, Hsp27 has a single highly conserved cysteine residue located at the dimer interface, which forms a disulfide bridge across the interface under oxidising conditions (Fig. S9). Our AUC data demonstrate that both αB-C ACD and Hsp27 ACD can form monomers in solution, but only in the absence of a disulfide bridge at the dimer interface (Fig. 3A-B, Fig. S15). To further test whether the monomer-dimer equilibrium affects the chaperone activity of the ACD we sought to directly compare the ability of Hsp27 ACD and αB-C ACD to inhibit apoC-II fibril rejoining. At a concentration of 12.8 μM, Hsp27 ACD was found to inhibit apoC-II fibril rejoining, but less effectively than αB-C ACD at the same concentration (Fig. 6A-B). However, in the presence of TCEP, Hsp27 ACD inhibited apoC-II fibril rejoining almost as effectively as αB-C ACD (Fig. 6A-B). Importantly, removing the disulfide from the Hsp27 ACD by mutating the cysteine to a serine residue (C137S) was found to exert the same effect as the reducing agent (Fig. 6C). Mutation of

the corresponding interface residue in αB-C ACD to a cysteine (E117C) was also found to reduce the ability of this construct to inhibit end-to-end joining, particularly at the lower concentration of 0.8 μM (Fig. 6E), which we previously demonstrated was close to the lower limit for observing an effect on fibril rejoining (Fig. 1F). Similarly, the effect of the C137S mutation on Hsp27 ACD was particularly evident at a concentration of 0.8 μM (Fig. 6F), despite being less pronounced at 12.8 μM (Fig. 6B-C).

Given these findings, we reasoned that disulfide crosslinking of the ACD dimer interface may reduce the ability of these proteins to inhibit apoC-II fibril formation and elongation. To further test this, full-length and ACD-only constructs of αB-C and Hsp27 were made with and without a cysteine residue at the interface. We confirmed, using mass spectrometry and non-reducing SDS-PAGE, that disulfide linked dimers are formed in the absence of reducing agents (Fig. S9). We then tested the abilities of all these constructs to inhibit apoC-II fibril formation using ThT assays in the presence or absence of the reducing agent TCEP. For all constructs tested, including the full-length constructs, the chaperone activity was enhanced by removing the intra-dimer disulfide bridge via mutagenesis or by using a reducing agent (Fig. 7A-D). We also examined the size distributions of the apoC-II fibrils formed in the presence of all these constructs with or without TCEP and found that the fibril size distributions were in excellent agreement with the results of the ThT assays (Fig. 7E-H). The fibril weight-average sedimentation coefficients were smaller when the fibrils were formed in the presence of a sHSP construct lacking an intra-dimer disulfide (WT αB-C, αB-C ACD, Hsp27 C137S, Hsp27 ACD C137S) as compared to fibrils formed in the presence of a sHSP construct containing a disulfide bridge (αB-C E117C, αB-C ACD E117C, WT Hsp27 or Hsp27 ACD). With the exception of full-length αB-C E117C + TCEP, the presence of the reducing agent exerted a similar effect on the resulting fibril size distributions as removing the disulfide via mutagenesis.

We also tested the chaperone activity of the full-length and ACD only constructs against α-synuclein fibril formation using ThT assays and pelleting assays (Fig. S16A-D). Similar to our observation with apoC-II fibrils, removal of the intra-dimer disulfide improved the chaperone activity of Hsp27 constructs against α-synuclein fibril formation. However, the opposite trend was observed for αB-C constructs, with the E117C mutation improving chaperone activity in these

assays. One possible explanation for this difference between αB-C and Hsp27 in the α-synuclein assays is that both αB-C ACD constructs co-precipitate with α-synuclein fibrils over the duration of the ThT assay, resulting in their depletion from the soluble phase, whereas both Hsp27 ACD constructs remain soluble (Fig. S16E). These observations are in contrast to those with apoC-II fibrils, where neither ACD construct stably associates with the fibrils [32].

– Discussion –

Though sHSPs have long been known to inhibit amyloid fibril formation, the mechanisms by which they do so remain somewhat enigmatic due to their structural heterogeneity and flexibility. Removal of the dynamic NTR and CTR enabled high resolution structures of the ACD to be determined [9,11,12,20,22,42]. Consequently, sHSP oligomers have generally been regarded to act as storage forms, while the dimers, formed by the ACD, are proposed to be the predominant chaperone active species [12,22,43,44]. Because sHSPs have a strong propensity to dimerise, the chaperone function(s) of the monomers have mostly been overlooked. In this work, we identified novel chaperone properties of the ACD of two sHSPs, αB-C and Hsp27, namely their ability to bind to the ends of growing amyloid fibrils. While both dimeric and monomeric sHSPs contribute to chaperone activity and transient amyloid fibril binding, conditions that favour the αB-C ACD monomer were shown to increase its ability to interact with apoC-II amyloid fibrils, and to inhibit fibril formation and end-to-end joining. Based on these results, we propose a model for the transient interaction of αB-C ACD monomer with apoC-II amyloid fibril ends whereby monomeric forms of the ACD may have an enhanced ability to form transient interactions with elongating fibrils through binding to the structured ends of fibrils via the exposed, complementary intra-dimer interface (Fig. 8). This model is in agreement with recently published work investigating the monomer-dimer equilibrium and chaperone activity of Hsp27 ACD [41]. While the majority of this work focused on the ACD, our experiments with full-length constructs support the notion that dynamics at the dimer interface regulate the chaperone activity of full-length sHSPs in a similar manner.

A major finding of this work is the demonstration that αB-C ACD forms transient interactions with apoC-II amyloid fibrils, resulting in the inhibition of fibril elongation and end-to-end joining. These findings complement our earlier work, which showed that full-length αB-C and Hsp27 form stable associations with amyloid fibrils, mediated by the flexible NTR and CTR, and that these interactions promote both fibril tangling and fibril dissociation [32]. Therefore, the interactions of sHSPs with amyloid fibrils are highly complex and have multiple effects on fibril dynamics. An interaction between αB-C ACD and fibril ends was previously proposed based on the observation that a construct lacking the NTR inhibited seeded Aβ(1-40) amyloid formation as effectively as full-length αB-C [20], however no direct evidence for this hypothesis was presented. To the best

of our knowledge, the work presented here is the first to provide direct evidence of an interaction between the ACD of sHSPs and amyloid fibrils. This finding is important because fibril fragments/seeds are a major mediator of cytotoxicity *in vivo* due to their ability to propagate protein aggregation throughout and between cells. Fibril end-binding therefore represents a potent mechanism that sHSPs use to inhibit the propagation of aggregates and the toxicity associated with this process. This fibril end-binding is likely conserved in the context of the full-length protein as evidenced by our AUC-derived fibril size distributions and ThT assays. It is reasonable to assume that the ACD of sHSPs may also mediate an interaction with other types of protein aggregates that are enriched with β-structure, such as pre-fibrillar oligomers, however further studies would be required to confirm this.

Another finding presented here is the solution-phase characterisation of the monomer-dimer equilibrium of αB-C ACD at physiological and near-physiological pH using both AUC and NMR. We find that though the ACD dimer is predominant at neutral pH and micromolar concentrations, the monomer is detectable by both techniques: AUC analysis yields a sedimentation coefficient distribution left-shifted relative to disulfide-cross-linked dimers and NMR reveals a minor population with an alternate poorly structured conformation in equilibrium with the ACD dimer. In agreement with previous work, the equilibrium between monomers and dimers is shifted towards the monomer at lower pH [39]. Destabilisation of the αB-C ACD dimer in a pH-dependent manner may be due to histidine residues located at and near the dimer interface [39].

The extent to which monomeric forms of full-length αB-C and Hsp27 are populated both *in vitro* and *in vivo* remains an open question. The exchange of monomers from full-length αB-C oligomers was suggested initially based on the detection of both odd- and even-numbered αB-C oligomers via native MS [45]. Importantly, the abundance of odd-numbered oligomers was found to increase with decreasing pH [13], consistent with the pH-dependent change in the monomer-dimer equilibrium we observed using AUC experiments. Models for odd-numbered oligomers have also been proposed based on cryo-EM data [14]. Additionally, dimers and monomers of αB-C ACD were both detected in the gas-phase using native MS, while only dimers were detected for αB-C ACD E117C [12]. Likewise, only dimers were detected for Hsp27 ACD via native MS whereas both monomers and dimers were detected upon disulfide reduction or removal of the disulfide

using mutagenesis [41]. Native MS also revealed that a full-length Hsp27 construct partially dissociates into monomers in the presence of a reducing agent [46]. Overall, these findings indicate that both pH and disulfide cross-linking regulate the oligomeric sub-structure of sHSPs as well as the stability of ACD-only dimers.

How then does a reduction in pH and/or removal of the intra-dimer disulfide enhance the chaperone activity of an oligomeric, full-length sHSP? One possibility is that destabilisation of the dimer interface enhances the exchange of monomers from oligomers, as has been proposed based on native MS [13,47]. Another explanation is that the conformation of sHSP subunits within the oligomer under conditions of reduced pH (or disulfide-reduction in the case of Hsp27) is altered in such a way that there is an increase in the exposure of the intra-dimer interface, which may function as an additional client binding site, as depicted in Fig. 8. Alterations to the conformational ensemble of oligomeric sHSPs in response to phosphorylation of the N-terminal region or changes in pH or temperature have already been found to regulate chaperone activity [39,46–49]. For example, phosphorylation of three serine residues in the N-terminal region of αB-C reduces the average oligomeric size, increases the flexibility and solvent exposure of the N-terminal region, and enhances chaperone activity [48]. Our results indicate that, in addition to the N-terminal region, the β6+7 strand that forms the dimer interface may be an additional client binding site regulated by conformational dynamics. Supporting this theory, the dimer interface of Hsp27 ACD was recently identified as the region of highest chemical shift perturbation in the presence of the amyotrophic lateral sclerosis-associated RNA-binding protein, fused in sarcoma (FUS) [50]. From a structural perspective, the intra-dimer interface is an ideal candidate for forming interactions with the ends of fibrils. The intra-dimer interface is the longest β-strand in the ACD. The plasticity of this interface has been demonstrated by the crystallization of αB-C ACD in 3 different registers of the β6+7 strand at the dimer interface [9,11,12] and also by a crystal structure of Hsp27 ACD in which the β4 strand forms an interface with the β6+7 strand [51]. These observations suggest that the β6+7 strand can form hydrogen bonding interactions with unpaired β-strands in a promiscuous manner, making it an excellent candidate for binding to fibril ends. In odd-numbered sHSP oligomers, at least one dimer interface would be more readily accessible for interactions with client proteins, including growing fibrils. Thus, the specific sub-structure of the oligomer would then define the accessibility of a client binding site such as the β6+7 strand.

Here we found that Hsp27 was a more effective chaperone in the reduced state compared to the oxidised state, yet Hsp27 is a cytosolic protein, meaning that the intra-dimer disulfide may be expected to be in the reduced state *in vivo*. Nevertheless, the cysteine residue located at the intra-dimer interface is highly conserved in Hsp27 orthologs. Cysteine residues have an unusual pattern of conservation where, relative to other residues, cysteine is either very poorly conserved or very highly conserved [52]. Furthermore, cysteine residues when spatially clustered have been found to be more highly conserved than isolated cysteine residues. Highly conserved cysteine residues are predicted to be located at functionally important sites, such as at catalytic sites, or to be involved in stabilizing the structure of a protein through disulfide bond formation. Hsp27 is not known to possess catalytic activity, therefore it is likely that the cysteine residue located at the dimer interface is either functionally important or involved in stabilizing the structure of Hsp27 through disulfide bond formation, or both. There is some existing evidence supporting both hypotheses. Firstly, Hsp27 can form disulfide cross-linked dimers intracellularly under conditions of oxidative stress [53,54]. Unsurprisingly, disulfide bond formation was shown to stabilize Hsp27 against urea-induced denaturation [54] and thermally induced changes in its quaternary structure [55]. Conversely, intra-dimer disulfide crosslinking of Hsp27 was found to either minimally impact its chaperone activity [54,56] or to decrease its chaperone activity, depending on the client tested [41,55]. These findings raise the question as to why the cysteine residue is so highly conserved. The answer to this question likely necessitates a broader understanding of the functions of Hsp27 in a cellular context. Aside from its function as a molecular chaperone, Hsp27 upregulates intracellular glutathione and increases the activity of enzymes involved in the pentose phosphate pathway such as glucose-6-phosphate dehydrogenase [57]. These functions increase the reductive capacity of the cell and decrease intracellular reactive oxygen species (ROS). Mutation of the conserved cysteine residue in Hsp27 reduced cellular resistance to conditions of oxidative stress such as exposure to hydrogen peroxide [53,56,57]. Moreover, the anti-apoptotic binding of Hsp27 to cytochrome c was found to be dependent on the lone cysteine residue of Hsp27 [58]. Based on these studies it is plausible that under basal conditions in the absence of oxidative stress, Hsp27 chaperones various clients in its oligomeric, dimeric or monomeric form. Against some clients, for example amyloidogenic clients, the monomeric form appears to have an enhanced chaperone activity. A second function of Hsp27 is to serve as a sensor for the intracellular redox

state and reduce intracellular ROS. Thus, under conditions of oxidative stress, the primary intracellular role of Hsp27 may be to inhibit apoptosis and/or maintain a reducing environment within the cell [57]. This is significant because there is a strong correlation between the accumulation of ROS and a reduction in life span [59,60]. Increased levels of oxidative stress are also evident in AD and PD brains [61,62]. A holistic understanding of the functional importance of the cysteine residue and its oxidized or reduced state relies on further *in vivo* studies, particularly those examining the chaperone activity and antioxidant properties of Hsp27 under various redox conditions.

Overall, this work provides novel evidence for a specific interaction between the ACD of two human sHSPs and amyloid fibrils. This interaction is dependent on the monomer-dimer equilibrium, suggesting that the intra-dimer interface may be an important client binding site. These findings improve the structure-function relationship of sHSPs and have important implications for understanding the role of sHSPs in the pathogenesis of diseases involving amyloid fibril formation.

– Materials and methods –

A pET11a vector encoding for apoC-II expression, pET24a vectors encoding human αB-C ACD (residues 68–153), αB-C ACD E117C, Hsp27 ACD (residues 84–176), Hsp27 ACD C137S or αB-C and a pET3a vector encoding human Hsp27 were used for expression of the proteins. Tobacco etch virus protease with L56V and S135G stabilizing mutations was expressed and purified according to the methods developed by Cabrita et al. [63]. All proteins were purified according to protocols outlined elsewhere [32].

Isotope labelling of αB-C ACD:

A 100 x micronutrient mixture was prepared with the following components: 6g/L FeSO4, 6 g/L CaCl2, 1.2 g/L MnCl2, 0.8 g/L CoCl2, 0.7 g/L ZnSO4, 0.3 g/L CuCl2, 20 mg/L H3BO3, 0.25 g/L (NH4)6Mo7)24.4H2O and 5 g/L EDTA. Uniformly 15N-labeled αB-C ACD was expressed in BL21 DE3 *E. coli* cells using the 322 autoinduction protocol [64]. 2 L cultures were grown at 37 °C, 200 rpm in N-5052 media (50 mM K2HPO4, 50 mM KH2PO4, 5 mM Na2SO4, 2 mM MgSO4, 0.5% (w/v) glycerol, 0.05% (w/v) glucose, 0.2% (w/v) lactose and 0.6 x micronutrient mixture (6 mL/L)) containing $^{15}NH_4Cl$ (1 g/L) as the sole nitrogen source for 8 hours and at 16°C until a static OD was reached, at which point the cells were harvested by centrifugation. Purification was performed in an identical manner to that of unlabelled αB-C ACD [32].

Fibril sonication:

Ultrasonication has been well established as a method of fragmenting amyloid fibrils, resulting in fibril populations with uniform lengths. Furthermore, sonication has previously been demonstrated to reduce the lengths (and therefore increase the number of free fibril ends) of apoC-II fibrils via SV-AUC [35]. For SV-AUC or NMR experiments using fragmented fibrils apoC-II were sonicated at an amplitude of 20% (1.6 mm mictrotip probe, Q500 sonicator, QSonica, USA) on ice for fourteen 30 second on/off-pulses.

ApoC-II ThT fibril formation assays:

ApoC-II fibril formation assays were performed as described previously [32]. Briefly, apoC-II was rapidly diluted from guanidine hydrochloride stocks into fibrillation buffer (0.1 M sodium phosphate, pH 7.4, 0.1% sodium azide) to generate monomeric stocks immediately prior to each

experiment. These monomeric stocks were aliquoted into wells of a clear, flat-bottomed 96-well tissue culture plate to a final concentration of 56 uM. For ThT assays, 10 ul of a 100 uM ThT stock (prepared in 0.1 M sodium phosphate, pH 7.4, 0.1% sodium azide) was also added along with the required volume of the relevant sHSP or a matching volume of buffer. The total assay volume in each case was 100 uL. The final concentration of guanidine hydrochloride was 66 mM. The plates were incubated in a FLUOstar® Omega microplate reader (BMG Labtech, Melbourne, Australia) at 30 °C without shaking for up to 200 h.

SV-AUC analysis:

SV-AUC analysis was performed as described previously [32]. Briefly, samples of 380 µL were loaded into one sector of a 12-mm double-sector charcoal-filled epon centrepiece and 400 µL of the relevant reference solution was loaded into the other sector of the cell. Radial absorbance scans were taken using an XL-1 analytical ultracentrifuge (Beckman Coulter, CA, USA) equipped with a Ti50 rotor at 20°C, collecting scans at 4 min intervals with a radial step size of 0.003 cm. All SV-AUC experiments of apoC-II fibrils formed with sHSP constructs 168 hours were analysed at a rotor speed of 8,000 rpm (5,161 x *g*) with detection wavelengths between 275 – 290 nm. For all of these experiments, the c(s) distributions were obtained by fitting the data using SEDFIT [65] with the hydrodynamic scaling law derived from the worm-like chain regularization by second derivative [38]. Weight-average fibril sizes were approximated from their weight-average sedimentation coefficients using a sedimentation coefficient vs MW relationship previously derived [38]. SV-AUC data for all ACD-only constructs in the absence of apoC-II fibrils were analysed at a rotor speed of 50,000 rpm (201,600 x *g*) with detection wavelengths of between 225 – 280 nm. The continuous sedimentation coefficient distribution c(s) model using regularization by maximum entropy was used to fit SV-AUC data for all of these experiments [65]. SV-AUC experiments of fragmented apoC-II fibrils were analysed at a rotor speed of 10,000 rpm (8,064 x g) with detection wavelengths of between 275 – 290 nm. The apparent sedimentation coefficient distributions (ls-g*(s)) were obtained by least-squares boundary modelling using Tikhonov-Phillips regularization by second derivative [65,66]. For all SV-AUC data presented, a regularisation parameter of p = 0.95 was used with 250 sedimentation coefficient increments over the selected sedimentation coefficient range (which necessarily varies for different experiments). The area under peaks in all the c(s) distributions presented here were obtained by integrating the

distributions over the specified sedimentation coefficient range using the SEDFIT software [65]. The buffer density (ρ), buffer viscosity (η) and partial specific volume ($\bar{v}$) used for the analysis of all sHSP constructs analysed in isolation of apoC-II fibrils were calculated using the SEDNTERP software (version 14.6e) [67]. Estimates of the MW of sedimenting particles were obtained using the SEDFIT software, which employs the Svedberg relationship to relate the molar mass of a sedimenting particle with its sedimentation coefficient, frictional coefficient and partial-specific volume, in a solvent with a given density [65]. SV-AUC data for αB-C ACD at pH 6.0 were integrated from 0.5 – 5 S and weight average sedimentation coefficients were fitted to a monomer-dimer self-association model using SEDPHAT [68] with $S_{20,w}$ constraints of 1.2 – 1.35 S for the monomer and 1.6 – 1.8 S for the dimer, respectively.

Transmission electron microscopy:

Carbon-coated Formvar 300 mesh copper grids were glow-discharged under reduced atmospheric pressure for 30 s at 25 mA. ApoC-II samples were diluted to 11 uM in distilled H_2O. 4 ul aliquots of diluted samples were adsorbed onto the grid for 60 s. The samples were blotted using filter paper, and the grids were stained twice with 4 ml of 2% potassium phosphotungstate, pH 6.8, and air-dried. The grids were observed at the Bio21 Institute Advanced Microscopy Facility under a Talos L120C TEM (Thermo Fisher Scientific) operating at 120 kV. The images were captured digitally using a Ceta 16M digital camera (Thermo Fisher Scientific).

Nuclear magnetic resonance spectroscopy:

For all ^{15}N-HSQC experiments in which pre-formed apoC-II fibrils were added to ^{15}N αB-C ACD, ^{15}N αB-C ACD was prepared in sodium phosphate buffer (50 mM sodium phosphate, pH 7.4 or 6.5, 0.02% sodium azide, 1 mM EDTA, 10% D_2O) and reference spectra were collected first. Fibrils were prepared as described for the ThT assays with ThT omitted from the buffers. Fibrils were twice pelleted by centrifugation at 385,000 x g for 30 minutes at room temperature (TLA-100 rotor OptimaMax centrifuge, Beckman Coulter). After the first spin, fibrils were resuspended in an equal volume of buffer matching that of the buffer used for the reference spectra, to ensure complete buffer matching. After the second spin, the fibrils were resuspended directly into the sample containing ^{15}N αB-C ACD used for the collection of the reference spectra. ^{15}N-HSQC spectra were then recorded for this sample, containing both ^{15}N αB-C ACD and fibrils. To

obtain spectra for ^{15}N αB-C ACD in the presence of fragmented fibrils, the sample containing ^{15}N αB-C ACD and the resuspended fibrils was sonicated according to the protocol outlined above. To test whether the process of sonication affected the ^{15}N-HSQC spectra of ^{15}N αB-C ACD alone, samples containing ^{15}N αB-C ACD were also sonicated in the absence of fibrils prior to data acquisition and the resulting spectra were compared to spectra obtained prior to sonication. For experiments in which HSQC spectra were obtained for ^{15}N αB-C ACD at multiple different pHs, a reference spectrum was initially recorded at pH 7.4. The sample was subsequently recovered and HCl (1 M) was titrated into the sample to achieve the desired pH. Adjusting the pH in this way required the addition of 2 – 4 μL of 1 M HCl, thus the effect of dilution is negligible.

The majority of NMR results presented in this work are short experiments with a duration of up to 6 hours. However, to test the stability of ^{15}N αB-C ACD over longer timescales, HSQCs were recorded on samples of ^{15}N αB-C ACD (1 mM) at pH 7.4 and pH 6.5 before and after incubation at 35°C for up to three days. Comparisons of the spectra obtained prior to and after incubation revealed no major differences in peak positions or peak intensities, indicating that αB-C ACD is stable in these conditions and over the timescales of the experiments presented in this work.

NMR spectra were obtained on either a Bruker Avance II 800 MHz spectrometer equipped with TXI cryoprobe and a single axis field gradient (Gz) or a Bruker Avance HDIII 700 MHz spectrometer. All spectra were recorded at 298 K unless stated otherwise. Generally, 16 scans were collected per FID, however for spectra acquired at 25 μM, 64 scans were collected. A ^{15}N frequency of 70.94 MHz or 81.08 MHz was used for the 700 MHz and 800 MHz spectrometers, respectively. 1024 and between 100 to 150 complex data points were used for ^{1}H and ^{15}N, respectively. The spectral width was 12.02 and 30.00 ppm for ^{1}H and ^{15}N, respectively. NMR spectra were processed using NMRPipe [69] and analysed in NMRFAM-SPARKY [70]. All spectra were phased as well as possible using nmrDraw in NMRPipe, however, spectra have generally been plotted at low contour levels in order to view peaks with low signal intensities. In addition to this, some peaks undergo peak-doubling in a pH dependent manner. In some instances, these factors result in spectra that appear to be poorly phased. H chemical shifts were referenced indirectly using water proton signals in the NMRPipe software. ^{15}N chemical shifts were referenced using the ^{15}N/^{1}H ratio as described previously [71]. Chemical shift perturbations were calculated using [72]:

$$\Delta\delta ppm = \left(\left(\Delta^{1}H\right)^{2} + \left(0.154\Delta^{15}N\right)^{2}\right)^{\frac{1}{2}} \quad (Eq.\,1)$$

– Accession numbers –

Backbone amide resonance assignments for αB-C ACD (residues 68-153) were obtained from published assignments (BMRB: 25527) [39].

– Acknowledgements –

E.E.S is a recipient of an Australian Government Research Training Program Scholarship. M.D.W.G is the recipient of an Australian Research Council Future Fellowship (project number FT140100544). We thank Shenggen Yao for assistance with collection of NMR spectra. We also acknowledge the Melbourne Magnetic Resonance Facility, the Melbourne Protein Characterisation Platform, the Ian Holmes Imaging Centre, and the Melbourne Mass Spectrometry and Proteomics Facility, at the Bio21 Molecular Science and Biotechnology Institute, for technical support.

– References –

[1] C. Garrido, C. Paul, R. Seigneuric, H.H. Kampinga, The small heat shock proteins family: The long forgotten chaperones, The International Journal of Biochemistry & Cell Biology. 44 (2012) 1588–1592. https://doi.org/10.1016/j.biocel.2012.02.022.

[2] J. den Engelsman, V. Keijsers, W.W. de Jong, W.C. Boelens, The Small Heat-shock Protein αB-Crystallin Promotes FBX4-dependent Ubiquitination, J. Biol. Chem. 278 (2003) 4699–4704. https://doi.org/10.1074/jbc.M211403200.

[3] S.J. Kolb, P.J. Snyder, E.J. Poi, E.A. Renard, A. Bartlett, S. Gu, S. Sutton, W.D. Arnold, M.L. Freimer, V.H. Lawson, J.T. Kissel, T.W. Prior, Mutant small heat shock protein B3 causes motor neuropathy: utility of a candidate gene approach, Neurology. 74 (2010) 502–506. https://doi.org/10.1212/WNL.0b013e3181cef84a.

[4] P. Vicart, A. Caron, P. Guicheney, Z. Li, M.C. Prévost, A. Faure, D. Chateau, F. Chapon, F. Tomé, J.M. Dupret, D. Paulin, M. Fardeau, A missense mutation in the alphaB-crystallin chaperone gene causes a desmin-related myopathy, Nat. Genet. 20 (1998) 92–95. https://doi.org/10.1038/1765.

[5] D.A. Haley, J. Horwitz, P.L. Stewart, The small heat-shock protein, αb-crystallin, has a variable quaternary structure, Journal of Molecular Biology. 277 (1998) 27–35. https://doi.org/10.1006/jmbi.1997.1611.

[6] J. Behlke, G. Lutsch, M. Gaestel, H. Bielka, Supramolecular structure of the recombinant murine small heat shock protein hsp25, FEBS Letters. 288 (1991) 119–122. https://doi.org/10.1016/0014-5793(91)81016-2.

[7] K.K. Kim, R. Kim, S.-H. Kim, Crystal structure of a small heat-shock protein, Nature. 394 (1998) 595. https://doi.org/10.1038/29106.

[8] R.L. van Montfort, E. Basha, K.L. Friedrich, C. Slingsby, E. Vierling, Crystal structure and assembly of a eukaryotic small heat shock protein, Nature Structural Biology. 8 (2001) 1025–1030.

[9] C. Bagnéris, O.A. Bateman, C.E. Naylor, N. Cronin, W.C. Boelens, N.H. Keep, C. Slingsby, Crystal Structures of α-Crystallin Domain Dimers of αB-Crystallin and Hsp20, Journal of Molecular Biology. 392 (2009) 1242–1252. https://doi.org/10.1016/j.jmb.2009.07.069.

[10] E.V. Baranova, S. Beelen, N.B. Gusev, S.V. Strelkov, The taming of small heat-shock proteins: crystallization of the α-crystallin domain from human Hsp27, Acta Cryst F. 65 (2009) 1277–1281. https://doi.org/10.1107/S1744309109044571.

[11] A. Laganowsky, J.L.P. Benesch, M. Landau, L. Ding, M.R. Sawaya, D. Cascio, Q. Huang, C.V. Robinson, J. Horwitz, D. Eisenberg, Crystal structures of truncated alphaA and alphaB crystallins reveal structural mechanisms of polydispersity important for eye lens function, Protein Science. 19 (2010) 1031–1043. https://doi.org/10.1002/pro.380.

[12] G.K.A. Hochberg, H. Ecroyd, C. Liu, D. Cox, D. Cascio, M.R. Sawaya, M.P. Collier, J. Stroud, J.A. Carver, A.J. Baldwin, C.V. Robinson, D.S. Eisenberg, J.L.P. Benesch, A. Laganowsky, The structured core domain of B-crystallin can prevent amyloid fibrillation and associated toxicity, Proceedings of the National Academy of Sciences. 111 (2014) E1562–E1570. https://doi.org/10.1073/pnas.1322673111.

[13] A.J. Baldwin, H. Lioe, C.V. Robinson, L.E. Kay, J.L.P. Benesch, αB-Crystallin Polydispersity Is a Consequence of Unbiased Quaternary Dynamics, Journal of Molecular Biology. 413 (2011) 297–309. https://doi.org/10.1016/j.jmb.2011.07.016.
[14] N. Braun, M. Zacharias, J. Peschek, A. Kastenmüller, J. Zou, M. Hanzlik, M. Haslbeck, J. Rappsilber, J. Buchner, S. Weinkauf, Multiple molecular architectures of the eye lens chaperone αB-crystallin elucidated by a triple hybrid approach, (2011) 6.
[15] S. Jehle, B.S. Vollmar, B. Bardiaux, K.K. Dove, P. Rajagopal, T. Gonen, H. Oschkinat, R.E. Klevit, N-terminal domain of alphaB-crystallin provides a conformational switch for multimerization and structural heterogeneity, Proceedings of the National Academy of Sciences of the United States of America. 108 (2011) 6409–14. https://doi.org/10.1073/pnas.1014656108.
[16] S.P. Delbecq, J.C. Rosenbaum, R.E. Klevit, A Mechanism of Subunit Recruitment in Human Small Heat Shock Protein Oligomers, Biochemistry. 54 (2015) 4276–4284. https://doi.org/10.1021/acs.biochem.5b00490.
[17] M. Haslbeck, S. Weinkauf, J. Buchner, Small heat shock proteins: Simplicity meets complexity, J Biol Chem. 294 (2019) 2121–2132. https://doi.org/10.1074/jbc.REV118.002809.
[18] E. Basha, H. O'Neill, E. Vierling, Small heat shock proteins and α-crystallins: dynamic proteins with flexible functions, Trends in Biochemical Sciences. 37 (2012) 106–117. https://doi.org/10.1016/j.tibs.2011.11.005.
[19] D. Cox, E. Selig, M.D.W. Griffin, J.A. Carver, H. Ecroyd, Small Heat-shock Proteins Prevent α-Synuclein Aggregation via Transient Interactions and Their Efficacy Is Affected by the Rate of Aggregation, J. Biol. Chem. 291 (2016) 22618–22629. https://doi.org/10.1074/jbc.M116.739250.
[20] A. Mainz, J. Peschek, M. Stavropoulou, K.C. Back, B. Bardiaux, S. Asami, E. Prade, C. Peters, S. Weinkauf, J. Buchner, B. Reif, The chaperone [alpha]B-crystallin uses different interfaces to capture an amorphous and an amyloid client, Nature Structural and Molecular Biology. (2015) 898. https://doi.org/10.1038/nsmb.3108.
[21] Z. Liu, C. Wang, Y. Li, C. Zhao, T. Li, D. Li, S. Zhang, C. Liu, Mechanistic insights into the switch of αB-crystallin chaperone activity and self-multimerization, J. Biol. Chem. 293 (2018) 14880–14890. https://doi.org/10.1074/jbc.RA118.004034.
[22] R. Freilich, M. Betegon, E. Tse, S.-A. Mok, O. Julien, D.A. Agard, D.R. Southworth, K. Takeuchi, J.E. Gestwicki, Competing protein-protein interactions regulate binding of Hsp27 to its client protein tau, Nat Commun. 9 (2018). https://doi.org/10.1038/s41467-018-07012-4.
[23] H.E.R. Baughman, T.-H.T. Pham, C.S. Adams, A. Nath, R.E. Klevit, Release of a disordered domain enhances HspB1 chaperone activity toward tau, PNAS. (2020). https://doi.org/10.1073/pnas.1915099117.
[24] J. Lowe, M. Landon, I. Pike, I. Spendlove, H. Mcdermott, R. John Mayer, Dementia with β-amyloid deposition: involvement of αB-crystallin supports two main diseases, The Lancet. 336 (1990) 515–516. https://doi.org/10.1016/0140-6736(90)92075-S.
[25] T.F. Outeiro, J. Klucken, K.E. Strathearn, F. Liu, P. Nguyen, J.-C. Rochet, B.T. Hyman, P.J. McLean, Small heat shock proteins protect against α-synuclein-induced toxicity and

aggregation, Biochemical and Biophysical Research Communications. 351 (2006) 631–638. https://doi.org/10.1016/j.bbrc.2006.10.085.
[26] M.M.M. Wilhelmus, I. Otte-Höller, P. Wesseling, R.M.W.D. Waal, W.C. Boelens, M.M. Verbeek, Specific association of small heat shock proteins with the pathological hallmarks of Alzheimer's disease brains, Neuropathology and Applied Neurobiology. 32 (2006) 119–130. https://doi.org/10.1111/j.1365-2990.2006.00689.x.
[27] B. Raman, T. Ban, M. Sakai, S.Y. Pasta, T. Ramakrishna, H. Naiki, Y. Goto, C.M. Rao, αB-crystallin, a small heat-shock protein, prevents the amyloid fibril growth of an amyloid β-peptide and β2-microglobulin, Biochemical Journal. 392 (2005) 573–581. https://doi.org/10.1042/BJ20050339.
[28] C.A. Waudby, T.P.J. Knowles, G.L. Devlin, J.N. Skepper, H. Ecroyd, J.A. Carver, M.E. Welland, J. Christodoulou, C.M. Dobson, S. Meehan, The Interaction of αB-Crystallin with Mature α-Synuclein Amyloid Fibrils Inhibits Their Elongation, Biophysical Journal. 98 (2010) 843–851. https://doi.org/10.1016/j.bpj.2009.10.056.
[29] S.L. Shammas, C.A. Waudby, S. Wang, A.K. Buell, T.P.J. Knowles, H. Ecroyd, M.E. Welland, J.A. Carver, C.M. Dobson, S. Meehan, Binding of the Molecular Chaperone αB-Crystallin to Aβ Amyloid Fibrils Inhibits Fibril Elongation, Biophysical Journal. 101 (2011) 1681–1689. https://doi.org/10.1016/j.bpj.2011.07.056.
[30] K.J. Binger, H. Ecroyd, S. Yang, J.A. Carver, G.J. Howlett, M.D.W. Griffin, Avoiding the oligomeric state: αB-crystallin inhibits fragmentation and induces dissociation of apolipoprotein C-II amyloid fibrils, The FASEB Journal. 27 (2013) 1214–1222. https://doi.org/10.1096/fj.12-220657.
[31] D. Cox, D.R. Whiten, J.W.P. Brown, M.H. Horrocks, R.S. Gil, C.M. Dobson, D. Klenerman, A.M. van Oijen, H. Ecroyd, The small heat shock protein Hsp27 binds α-synuclein fibrils, preventing elongation and cytotoxicity, J. Biol. Chem. 293 (2018) 4486–4497. https://doi.org/10.1074/jbc.M117.813865.
[32] E.E. Selig, C.O. Zlatic, D. Cox, Y.-F. Mok, P.R. Gooley, H. Ecroyd, M.D.W. Griffin, N- and C-terminal regions of αB-crystallin and Hsp27 mediate inhibition of amyloid nucleation, fibril binding, and fibril disaggregation, J. Biol. Chem. (2020). https://doi.org/10.1074/jbc.RA120.012748.
[33] B. Mannini, R. Cascella, M. Zampagni, M. van Waarde-Verhagen, S. Meehan, C. Roodveldt, S. Campioni, M. Boninsegna, A. Penco, A. Relini, H.H. Kampinga, C.M. Dobson, M.R. Wilson, C. Cecchi, F. Chiti, Molecular mechanisms used by chaperones to reduce the toxicity of aberrant protein oligomers, PNAS. 109 (2012) 12479–12484. https://doi.org/10.1073/pnas.1117799109.
[34] F.C. Dehle, H. Ecroyd, I.F. Musgrave, J.A. Carver, αB-Crystallin inhibits the cell toxicity associated with amyloid fibril formation by κ-casein and the amyloid-β peptide, Cell Stress Chaperones. 15 (2010) 1013–1026. https://doi.org/10.1007/s12192-010-0212-z.
[35] K.J. Binger, C.L.L. Pham, L.M. Wilson, M.F. Bailey, L.J. Lawrence, P. Schuck, G.J. Howlett, Apolipoprotein C-II Amyloid Fibrils Assemble via a Reversible Pathway that Includes Fibril Breaking and Rejoining, Journal of Molecular Biology. 376 (2008) 1116–1129. https://doi.org/10.1016/j.jmb.2007.12.055.

[36] D.M. Hatters, C.E. MacPhee, L.J. Lawrence, W.H. Sawyer, G.J. Howlett, Human Apolipoprotein C-II Forms Twisted Amyloid Ribbons and Closed Loops, Biochemistry. 39 (2000) 8276–8283. https://doi.org/10.1021/bi000002w.
[37] D.M. Hatters, C.A. MacRaild, R. Daniels, W.S. Gosal, N.H. Thomson, J.A. Jones, J.J. Davis, C.E. MacPhee, C.M. Dobson, G.J. Howlett, The Circularization of Amyloid Fibrils Formed by Apolipoprotein C-II, Biophysical Journal. 85 (2003) 3979–3990. https://doi.org/10.1016/S0006-3495(03)74812-7.
[38] C.A. MacRaild, D.M. Hatters, L.J. Lawrence, G.J. Howlett, Sedimentation Velocity Analysis of Flexible Macromolecules: Self-Association and Tangling of Amyloid Fibrils, Biophysical Journal. 84 (2003) 2562–2569. https://doi.org/10.1016/S0006-3495(03)75061-9.
[39] P. Rajagopal, E. Tse, A.J. Borst, S.P. Delbecq, L. Shi, D.R. Southworth, R.E. Klevit, A conserved histidine modulates HSPB5 structure to trigger chaperone activity in response to stress-related acidosis, ELife; Cambridge. 4 (2015). http://dx.doi.org.ezp.lib.unimelb.edu.au/10.7554/eLife.07304.
[40] S. Jehle, B. van Rossum, J.R. Stout, S.M. Noguchi, K. Falber, K. Rehbein, H. Oschkinat, R.E. Klevit, P. Rajagopal, αB-Crystallin: A Hybrid Solid-State/Solution-State NMR Investigation Reveals Structural Aspects of the Heterogeneous Oligomer, Journal of Molecular Biology. 385 (2009) 1481–1497. https://doi.org/10.1016/j.jmb.2008.10.097.
[41] T.R. Alderson, J. Roche, H.Y. Gastall, D.M. Dias, I. Pritišanac, J. Ying, A. Bax, J.L.P. Benesch, A.J. Baldwin, Local unfolding of the HSP27 monomer regulates chaperone activity, Nat Commun. 10 (2019). https://doi.org/10.1038/s41467-019-08557-8.
[42] P. Rajagopal, Y. Liu, L. Shi, A.F. Clouser, R.E. Klevit, Structure of the α-crystallin domain from the redox-sensitive chaperone, HSPB1, J Biomol NMR. 63 (2015) 223–228. https://doi.org/10.1007/s10858-015-9973-0.
[43] H.E.R. Baughman, A.F. Clouser, R.E. Klevit, A. Nath, HspB1 and Hsc70 chaperones engage distinct tau species and have different inhibitory effects on amyloid formation, J. Biol. Chem. 293 (2018) 2687–2700. https://doi.org/10.1074/jbc.M117.803411.
[44] A.F. Clouser, H.E. Baughman, B. Basanta, M. Guttman, A. Nath, R.E. Klevit, Interplay of disordered and ordered regions of a human small heat shock protein yields an ensemble of 'quasi-ordered' states, ELife. 8 (n.d.). https://doi.org/10.7554/eLife.50259.
[45] J.A. Aquilina, J.L.P. Benesch, O.A. Bateman, C. Slingsby, C.V. Robinson, Polydispersity of a mammalian chaperone: Mass spectrometry reveals the population of oligomers in B-crystallin, Proceedings of the National Academy of Sciences. 100 (2003) 10611–10616. https://doi.org/10.1073/pnas.1932958100.
[46] B. Jovcevski, M.A. Kelly, A.P. Rote, T. Berg, H.Y. Gastall, J.L.P. Benesch, J.A. Aquilina, H. Ecroyd, Phosphomimics Destabilize Hsp27 Oligomeric Assemblies and Enhance Chaperone Activity, Chemistry & Biology. 22 (2015) 186–195. https://doi.org/10.1016/j.chembiol.2015.01.001.
[47] J.A. Aquilina, J.L.P. Benesch, L.L. Ding, O. Yaron, J. Horwitz, C.V. Robinson, Phosphorylation of αB-Crystallin Alters Chaperone Function through Loss of Dimeric Substructure, J. Biol. Chem. 279 (2004) 28675–28680. https://doi.org/10.1074/jbc.M403348200.
[48] J. Peschek, N. Braun, J. Rohrberg, K.C. Back, T. Kriehuber, A. Kastenmüller, S. Weinkauf, J. Buchner, Regulated structural transitions unleash the chaperone activity of αB-crystallin,

Proceedings of the National Academy of Sciences. 110 (2013) E3780–E3789. https://doi.org/10.1073/pnas.1308898110.
[49] D. Hayes, V. Napoli, A. Mazurkie, W.F. Stafford, P. Graceffa, Phosphorylation Dependence of Hsp27 Multimeric Size and Molecular Chaperone Function, J. Biol. Chem. 284 (2009) 18801–18807. https://doi.org/10.1074/jbc.M109.011353.
[50] Z. Liu, S. Zhang, J. Gu, Y. Tong, Y. Li, X. Gui, H. Long, C. Wang, C. Zhao, J. Lu, L. He, Y. Li, Z. Liu, D. Li, C. Liu, Hsp27 chaperones FUS phase separation under the modulation of stress-induced phosphorylation, Nature Structural & Molecular Biology. (2020) 1–10. https://doi.org/10.1038/s41594-020-0399-3.
[51] E.V. Baranova, S.D. Weeks, S. Beelen, O.V. Bukach, N.B. Gusev, S.V. Strelkov, Three-dimensional structure of α-crystallin domain dimers of human small heat shock proteins HSPB1 and HSPB6, J. Mol. Biol. 411 (2011) 110–122. https://doi.org/10.1016/j.jmb.2011.05.024.
[52] S.M. Marino, V.N. Gladyshev, Cysteine function governs its conservation and degeneration and restricts its utilization on protein surface, J Mol Biol. 404 (2010) 902–916. https://doi.org/10.1016/j.jmb.2010.09.027.
[53] C. Diaz-Latoud, E. Buache, E. Javouhey, A.-P. Arrigo, Substitution of the Unique Cysteine Residue of Murine Hsp25 Interferes with the Protective Activity of This Stress Protein Through Inhibition of Dimer Formation, Antioxidants & Redox Signaling. 7 (2005) 436–445. https://doi.org/10.1089/ars.2005.7.436.
[54] A. Zavialov, R. Benndorf, M. Ehrnsperger, V. Zav'yalov, I. Dudich, J. Buchner, M. Gaestel, The effect of the intersubunit disulfide bond on the structural and functional properties of the small heat shock protein Hsp25, International Journal of Biological Macromolecules. 22 (1998) 163–173. https://doi.org/10.1016/S0141-8130(98)00014-2.
[55] A.S. Chalova, M.V. Sudnitsyna, P.I. Semenyuk, V.N. Orlov, N.B. Gusev, Effect of disulfide crosslinking on thermal transitions and chaperone-like activity of human small heat shock protein HspB1, Cell Stress Chaperones. 19 (2014) 963–972. https://doi.org/10.1007/s12192-014-0520-9.
[56] N. Pasupuleti, M. Gangadhariah, S. Padmanabha, P. Santhoshkumar, R.H. Nagaraj, The role of the cysteine residue in the chaperone and anti-apoptotic functions of human Hsp27, J. Cell. Biochem. 110 (2010) 408–419. https://doi.org/10.1002/jcb.22552.
[57] A.-P. Arrigo, S. Virot, S. Chaufour, W. Firdaus, C. Kretz-Remy, C. Diaz-Latoud, Hsp27 Consolidates Intracellular Redox Homeostasis by Upholding Glutathione in Its Reduced Form and by Decreasing Iron Intracellular Levels, (n.d.) 19.
[58] J.M. Bruey, C. Ducasse, P. Bonniaud, L. Ravagnan, S.A. Susin, C. Diaz-Latoud, S. Gurbuxani, A.P. Arrigo, G. Kroemer, E. Solary, C. Garrido, Hsp27 negatively regulates cell death by interacting with cytochrome c, Nature Cell Biology. 2 (2000) 645–652.
[59] T. Finkel, N.J. Holbrook, Oxidants, oxidative stress and the biology of ageing, Nature. 408 (2000) 239–247. https://doi.org/10.1038/35041687.
[60] J.R. Vanfleteren, Oxidative stress and ageing in Caenorhabditis elegans, Biochemical Journal. 292 (1993) 605–608. https://doi.org/10.1042/bj2920605.
[61] K. Jomova, D. Vondrakova, M. Lawson, M. Valko, Metals, oxidative stress and neurodegenerative disorders, Mol Cell Biochem. 345 (2010) 91–104. https://doi.org/10.1007/s11010-010-0563-x.

[62] P. Jenner, C.W. Olanow, Understanding cell death in parkinson's disease, Annals of Neurology. 44 (1998) S72–S84. https://doi.org/10.1002/ana.410440712.
[63] L.D. Cabrita, D. Gilis, A.L. Robertson, Y. Dehouck, M. Rooman, S.P. Bottomley, Enhancing the stability and solubility of TEV protease using in silico design, Protein Science : A Publication of the Protein Society. 16 (2007) 2360–7. https://doi.org/10.1110/ps.072822507.
[64] F.W. Studier, Protein production by auto-induction in high density shaking cultures, Protein Expr Purif. 41 (2005) 207–34.
[65] P. Schuck, Size-distribution analysis of macromolecules by sedimentation velocity ultracentrifugation and lamm equation modeling, Biophys J. 78 (2000) 1606–19. https://doi.org/10.1016/S0006-3495(00)76713-0.
[66] P. Schuck, P. Rossmanith, Determination of the sedimentation coefficient distribution by least-squares boundary modeling, Biopolymers. 54 (2000) 328–341. https://doi.org/10.1002/1097-0282(20001015)54:5<328::AID-BIP40>3.0.CO;2-P.
[67] S.E. Harding, A.J. Rowe, J.C. Horton, Analytical ultracentrifugation in biochemistry and polymer science, Royal Society of Chemistry, Cambridge England, 1992.
[68] H. Zhao, G. Piszczek, P. Schuck, SEDPHAT – a platform for global ITC analysis and global multi-method analysis of molecular interactions, Methods. 76 (2015) 137–148. https://doi.org/10.1016/j.ymeth.2014.11.012.
[69] F. Delaglio, S. Grzesiek, G.W. Vuister, G. Zhu, J. Pfeifer, A. Bax, NMRPipe: A multidimensional spectral processing system based on UNIX pipes, J Biomol NMR. 6 (1995) 277–293. https://doi.org/10.1007/BF00197809.
[70] W. Lee, M. Tonelli, J.L. Markley, NMRFAM-SPARKY: enhanced software for biomolecular NMR spectroscopy, Bioinformatics. 31 (2015) 1325–1327. https://doi.org/10.1093/bioinformatics/btu830.
[71] D.S. Wishart, C.G. Bigam, J. Yao, F. Abildgaard, H.J. Dyson, E. Oldfield, J.L. Markley, B.D. Sykes, 1H, 13C and 15N chemical shift referencing in biomolecular NMR, J Biomol NMR. 6 (1995) 135–140. https://doi.org/10.1007/BF00211777.
[72] A. Ayed, F.A. Mulder, G.S. Yi, Y. Lu, L.E. Kay, C.H. Arrowsmith, Latent and active p53 are identical in conformation, Nature Structural Biology. 8 (2001) 756–760.

– Figure Captions –

Figure 1. αB-C ACD inhibits apoC-II fibril elongation and end-to-end joining. A) ThT fibril formation kinetics of apoC-II (56 μM) alone (black) or with 12.8 μM WT αB-C (red) or αB-C ACD (green) at 30 °C. B) Fibril size distribution analysis using AUC apoC-II fibrils formed alone at 56 μM (black) or with 12.8 μM WT αB-C (red) or αB-C ACD (green) for 168 hours at 30 ºC. C-E) TEM of apoC-II fibrils formed alone (C) or with 12.8 μM WT αB-C (D) or αB-C ACD (E) for 168 hours at 30 ºC. F-G) Fibril size distribution analysis of apoC-II fibrils analysed immediately after sonication (F) or 72 hours after sonication (G) alone (black) or with 0.05 μM αB-C ACD (1:1120 molar ratio, red), 0.8 μM αB-C ACD (1:70 molar ratio, orange), 3.2 μM αB-C ACD (1:18 molar ratio, green) or 12.8 μM αB-C ACD (1:4 molar ratio, blue).

Figure 2. αB-C ACD preferentially interacts with fibril ends. A) ^{15}N-HSQC overlay of 50 μM αB-C ACD alone (red), in the presence of 1120 μM long apoC-II fibrils (green) or in the presence of 1120 μM short apoC-II fibrils (blue). Below the overlay are some zoomed regions of intense peaks arising from residues near the C-terminus and from side chains showing the loss of signal intensity of αB-C ACD in the presence of long and short apoC-II fibrils. B-E) Analysis of intensity ratios (I/I_0) where I_0 refers to the signal intensity of peaks in the spectra for 50 μM αB-C ACD alone in the absence of fibrils. B) I/I_0 for αB-C ACD in the presence of 1120 μM long apoC-II fibrils (green). C) I/I_0 for αB-C ACD in the presence of 1120 μM short apoC-II fibrils (blue). D) I/I_0 for αB-C ACD in the presence of 150 μM BSA (purple). E) I/I_0 for αB-C ACD alone after sonication. In each of B-E a red line depicts the signal intensity of 50 μM αB-C ACD alone. This entire experiment was replicated independently, yielding similar results, which are shown in Fig. S7.

Figure 3. Monomer–dimer exchange of αB-C ACD probed by NMR and AUC. A) AUC analysis of αB-C ACD at 12.8 μM at pH 7.4 (red), 6.5 (green) and 6.0 (blue). Also shown is 12.8 μM αB-C ACD E117C at pH 7.4 without TCEP (black) for comparison. B) AUC analysis of αB-C ACD E117C at 12.8 μM at pH 7.4 without TCEP (black) or with 2 mM TCEP (purple), or at pH 6 without TCEP (cyan) or with TCEP (pink). C) AUC analysis of αB-C ACD at pH 6.0 at the

following concentrations: 5 μM (black); 12.8 μM (red); 25 μM (green); 50 μM (blue); 100 μM (purple) or 200 μM (cyan). D) Weight average sedimentation coefficients were calculated from distributions in panel C (solid circles, coloured as in panel C) and fit to a monomer-dimer self-association model (black line) using SEDPHAT. E) Overlay of ^{15}N-HSQC of αB-C ACD at 25 μM pH 7.4 (red) and pH 6 (blue), revealing large spectral changes and the appearance of new peaks. E-H) CSP analysis of resonances in the ^{15}N HSQC spectra at pH 7.4 versus pH 6.0 for αB-C ACD at 25 μM (F), 50 μM (G), 100 μM (H) or 200 μM (I). Peaks that were no longer visible and/or that shifted too far for identification at pH 6.0 relative to pH 7.4 are indicated by solid red bars. This analysis reveals that two regions of αB-C ACD are no longer visible in the spectra at pH 6.0 relative to pH 7.4. These regions are the C-terminal end of β3 and the loop between β3 and β4 as well as the C-terminal end of β5, all of β6+7 and the loop between β6+7 and β8. These regions are indicated by a red arrow and in (J) mapped onto the crystal structure of the αB-C ACD dimer (PDB: 4m5s) in red. Regions that are visible in the spectra at both pH 7.4 and pH 6.0 are coloured purple.

Figure 4. A reduction in pH increases the extent of signal intensity loss of αB-C ACD in the presence of apoC-II fibrils. A) ^{15}N-HSQC of 50 μM αB-C ACD alone (red) or in the presence of 56 μM fragmented apoC-II fibrils (blue) at pH 7.4. B) ^{15}N-HSQC of 50 μM αB-C ACD alone (red) or in the presence of 56 μM fragmented apoC-II fibrils (blue) at pH 6.0. C) Analysis of intensity ratios (I/I_0) where I_0 and I refer to the signal intensity of peaks in the spectra shown in (A) for 50 μM αB-C ACD at pH 7.4 in the absence and presence of fragmented fibrils, respectively. D-E) Analysis of intensity ratios (I/I_0) where I_0 and I refer to the signal intensity of assigned peaks (black, D) or unassigned peaks (red, E) in the spectra shown in (B) for 50 μM αB-C ACD at pH 6.0 in the absence or presence of fragmented apoC-II fibrils, respectively.

Figure 5. Unassigned peaks corresponding to monomeric αB-C ACD are broadened to a greater extent than the assigned peaks. A) ^{15}N-HSQC overlay of 100 μM αB-C ACD alone (red) with 100 μM αB-C ACD in the presence of 1120 μM short apoC-II fibrils (blue). Analysis of intensity ratios (I/I_0) for B) assigned peaks and C) for unassigned peaks where I_0 and I are the signal

intensity of peaks in the spectra for 100 μM αB-C ACD in the absence and presence of fibrils, respectively.

Figure 6. Intradimer disulfide formation impairs the ability of ACD-only constructs of sHSPs to inhibit fibril end-to-end rejoining. In panels A-F apoC-II fibrils (56 μM) were formed for 168 hours at 30ºC prior to sonication and SV-AUC analysis. In each panel, the size distribution of apoC-II fibrils incubated alone after sonication is shown with a black line. In panels A-C the size distribution of apoC-II fibrils incubated with 2 mM TCEP after sonication is shown with a red line. AUC size distribution of fragmented apoC-II fibrils analysed immediately after sonication with A) 12.8 μM αB-C ACD (green) or with 12.8 μM αB-C ACD + TCEP (blue); B) 12.8 μM Hsp27 ACD (green) or with 12.8 μM Hsp27 ACD + TCEP (blue); C) 12.8 μM Hsp27 ACD C137S (green) or with 12.8 μM Hsp27 ACD C137S + TCEP (blue); D) 12.8 μM αB-C ACD (green) or with 12.8 μM αB-C ACD E117C (blue); E) 0.8 μM αB-C ACD (green) or with 0.8 μM αB-C ACD E117C (blue); and F) 0.8 μM Hsp27 ACD (green) or with 0.8 μM Hsp27 ACD C137S (blue).

Figure 7. Intradimer disulfide formation impairs the chaperone activity of αB-C and Hsp27. A-D) ThT kinetics of apoC-II fibril formation (56 μM) alone (black), in the presence of 2 mM TCEP (red), WT αB-C (A, red), αB-C ACD (B, red), WT Hsp27 (C, red), Hsp27 ACD (D, red), WT αB-C + TCEP (A, orange), αB-C ACD + TCEP (B orange), WT Hsp27 (C, orange), Hsp27 ACD (D, orange), αB-C E117C (A, green), αB-C ACD E117C (B, green), Hsp27 C137S (C, green), Hsp27 ACD C137S (D, green), αB-C E117C + TCEP (A, blue), αB-C ACD E117C + TCEP (B, blue), Hsp27 C137S + TCEP (C, blue), Hsp27 C137S + TCEP (D, blue). E-H) AUC fibril size distribution analysis of fibrils formed for 168 hours under the same conditions as shown in A-D and colour coded in the same way.

Figure 8. A model for the interaction of sHSP ACDs with amyloid fibrils. The ACD dimer (PDB 4M5S) is depicted in red in ribbon format using PyMOL. The ACD dimer exists in an equilibrium with ACD monomer at neutral pH. The dimer interface β-6+7 strand is likely to be

unfolded in the ACD monomer [41]. The ACD monomer may interact with amyloid fibrils (which are depicted as blue arrows representing β-sheets) at their ends to inhibit fibril elongation.

– Figures –

Figure 1

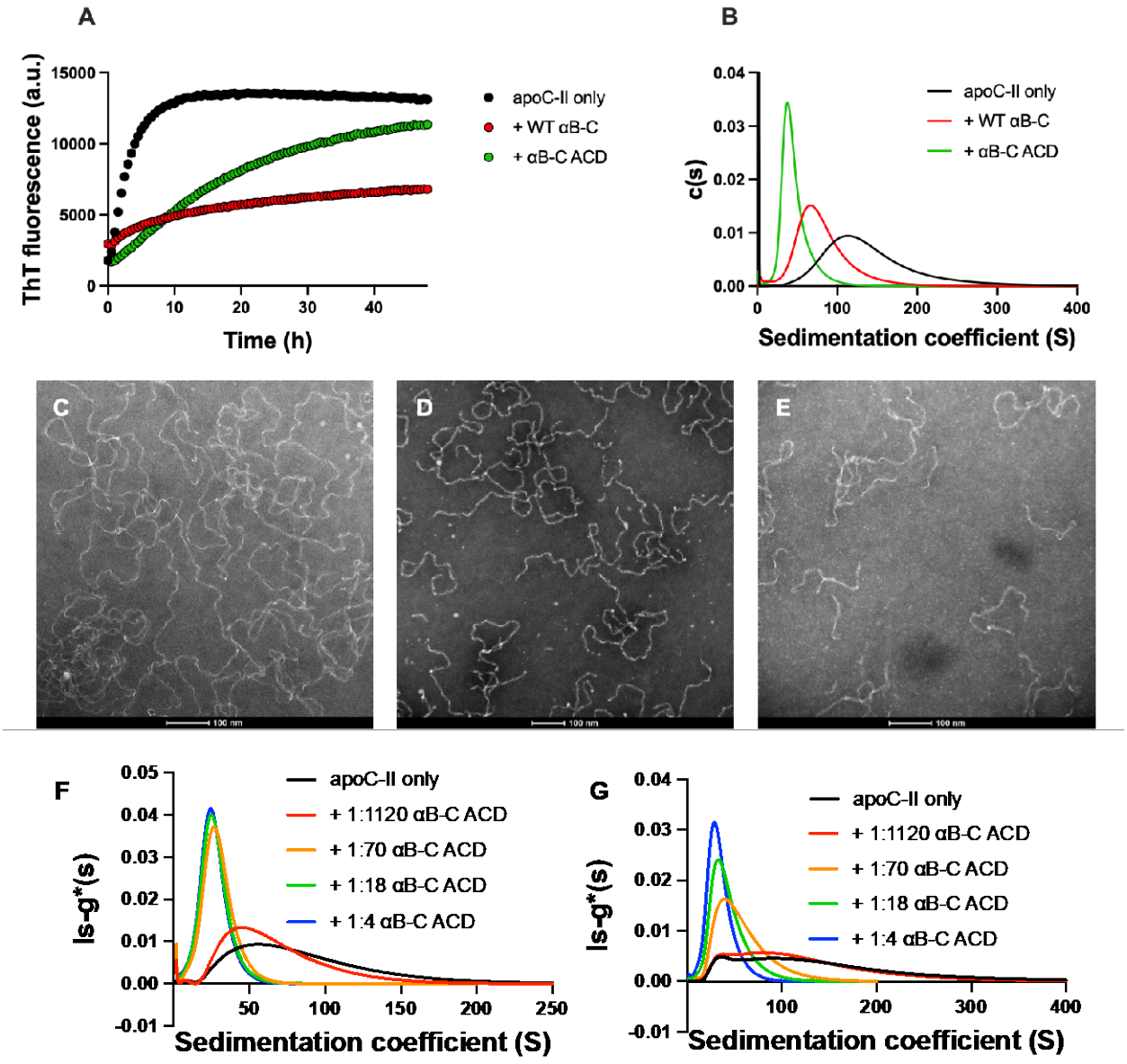

Figure 2

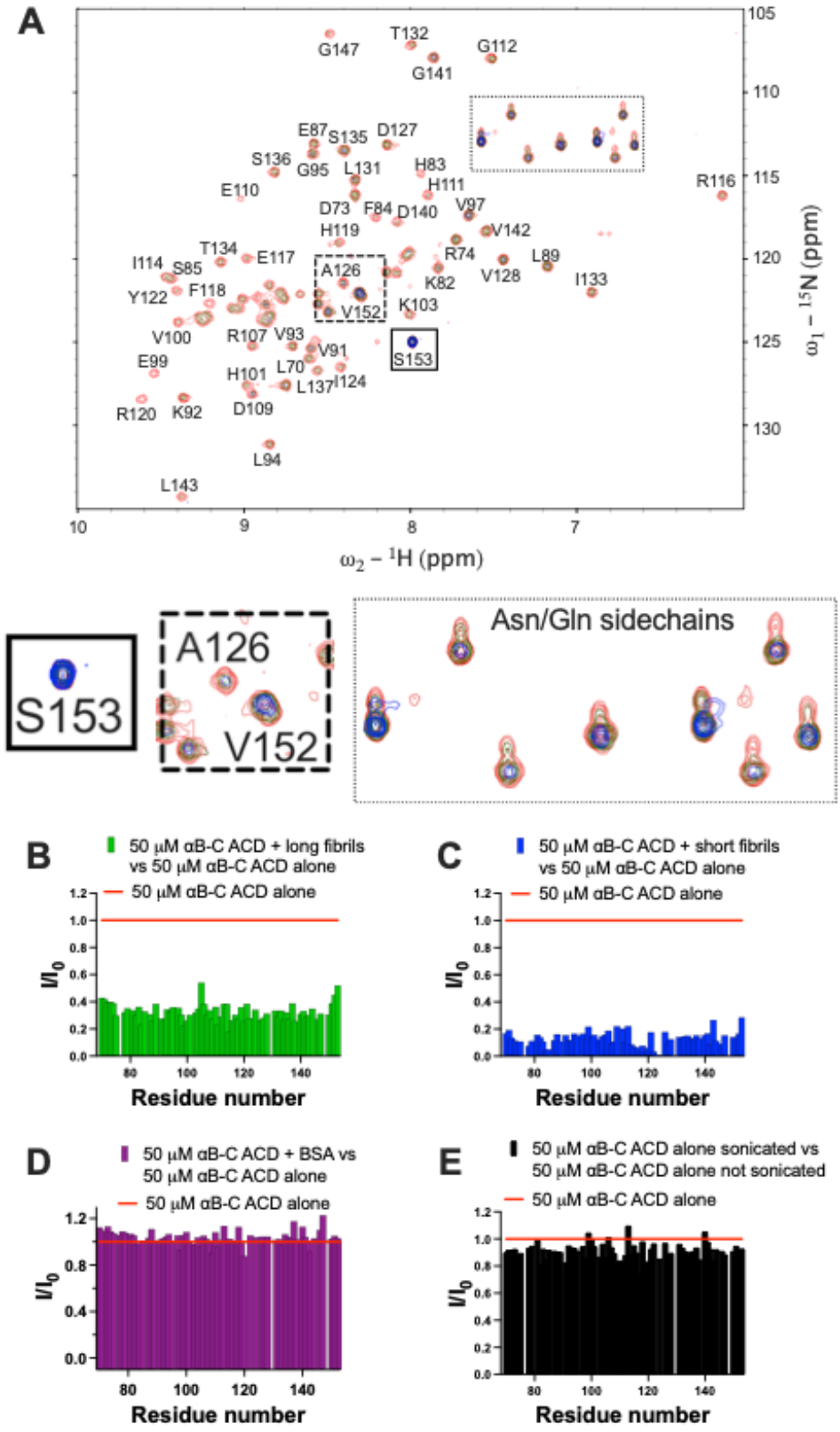
A
G147
T132
G112
G141
E87
S135
D127
S136
G95
L131
H83
H111
E110
R116
D73
F84
D140
V97
H119
V142
T134
E117
R74
L89
I114
S85
A126
K82
V128
I133
Y122
F118
V152
K103
V100
R107
V93
S153
V91
E99
H101
L70
L137
I124
R120
K92
D109
L94
L143
105
110
115
120
125
130
ω_1 – ^{15}N (ppm)
10
9
8
7
ω_2 – ^{1}H (ppm)
S153
A126
V152
Asn/Gln sidechains
B
50 μM αB-C ACD + long fibrils
vs 50 μM αB-C ACD alone
50 μM αB-C ACD alone
I/I0
Residue number
C
50 μM αB-C ACD + short fibrils
vs 50 μM αB-C ACD alone
50 μM αB-C ACD alone
I/I0
Residue number
D
50 μM αB-C ACD + BSA vs
50 μM αB-C ACD alone
50 μM αB-C ACD alone
I/I0
Residue number
E
50 μM αB-C ACD alone sonicated vs
50 μM αB-C ACD alone not sonicated
50 μM αB-C ACD alone
I/I0
Residue number

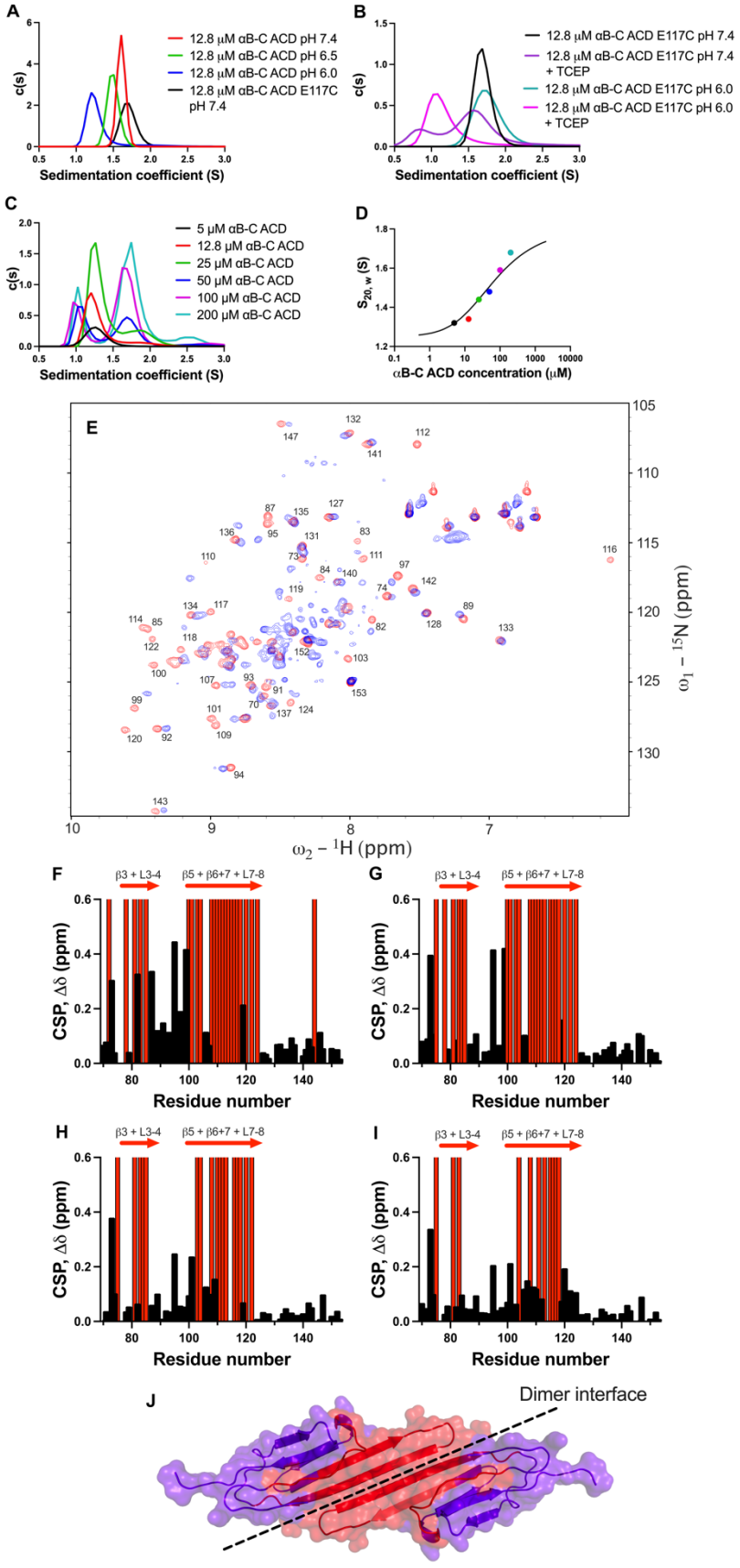
A
c(s)
Sedimentation coefficient (S)
12.8 μM αB-C ACD pH 7.4
12.8 μM αB-C ACD pH 6.5
12.8 μM αB-C ACD pH 6.0
12.8 μM αB-C ACD E117C pH 7.4
B
c(s)
Sedimentation coefficient (S)
12.8 μM αB-C ACD E117C pH 7.4
12.8 μM αB-C ACD E117C pH 7.4 + TCEP
12.8 μM αB-C ACD E117C pH 6.0
12.8 μM αB-C ACD E117C pH 6.0 + TCEP
C
c(s)
Sedimentation coefficient (S)
5 μM αB-C ACD
12.8 μM αB-C ACD
25 μM αB-C ACD
50 μM αB-C ACD
100 μM αB-C ACD
200 μM αB-C ACD
D
$S_{20,w}$ (S)
αB-C ACD concentration (μM)
E
ω_2 – ^{1}H (ppm)
ω_1 – ^{15}N (ppm)
F
G
H
I
β3 + L3-4
β5 + β6+7 + L7-8
CSP, Δδ (ppm)
Residue number
J
Dimer interface

Figure 4

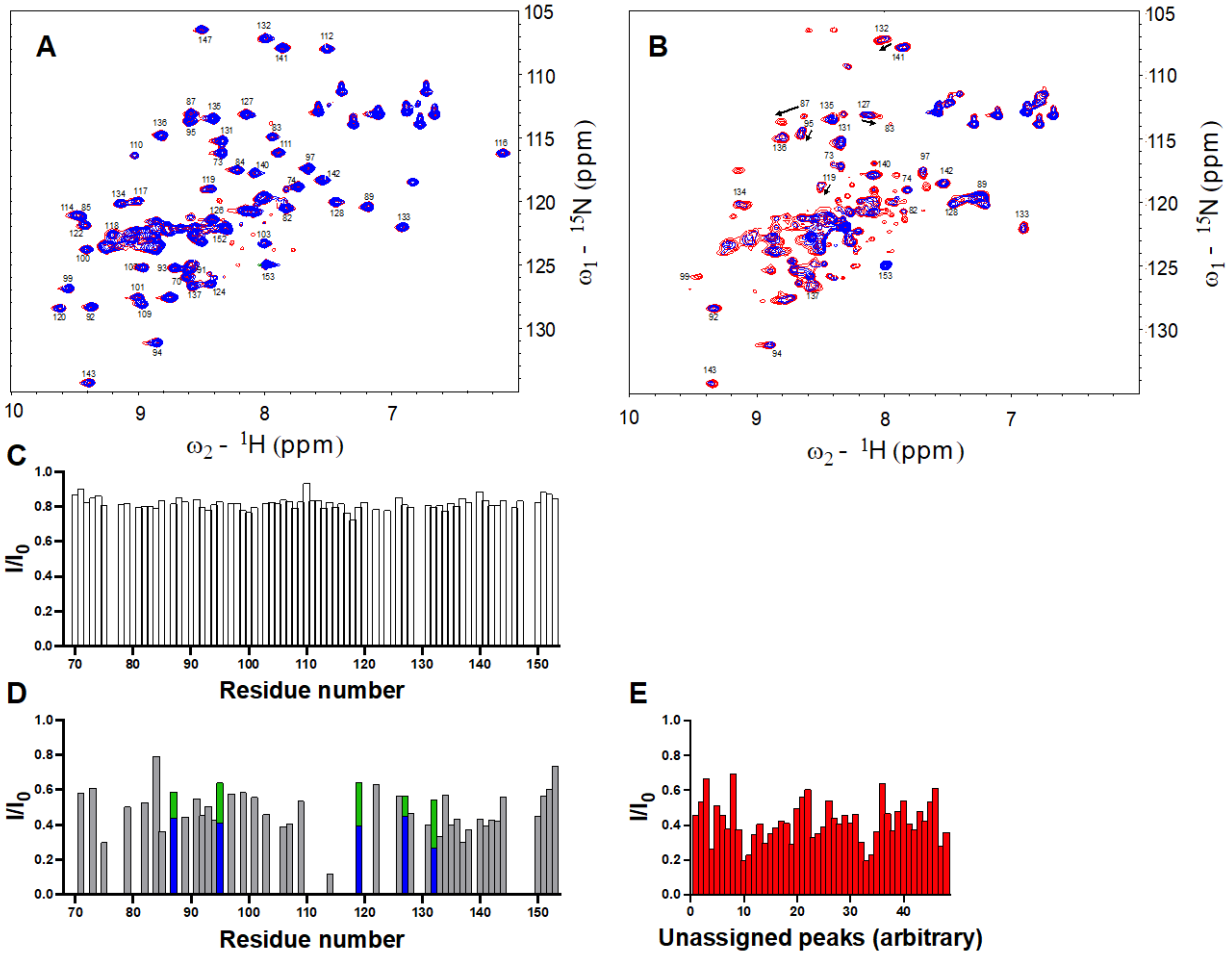
A
B
C
D
E
ω_2 - ^{1}H (ppm)
ω_1 - ^{15}N (ppm)
I/I$_0$
Residue number
Unassigned peaks (arbitrary)

Figure 5

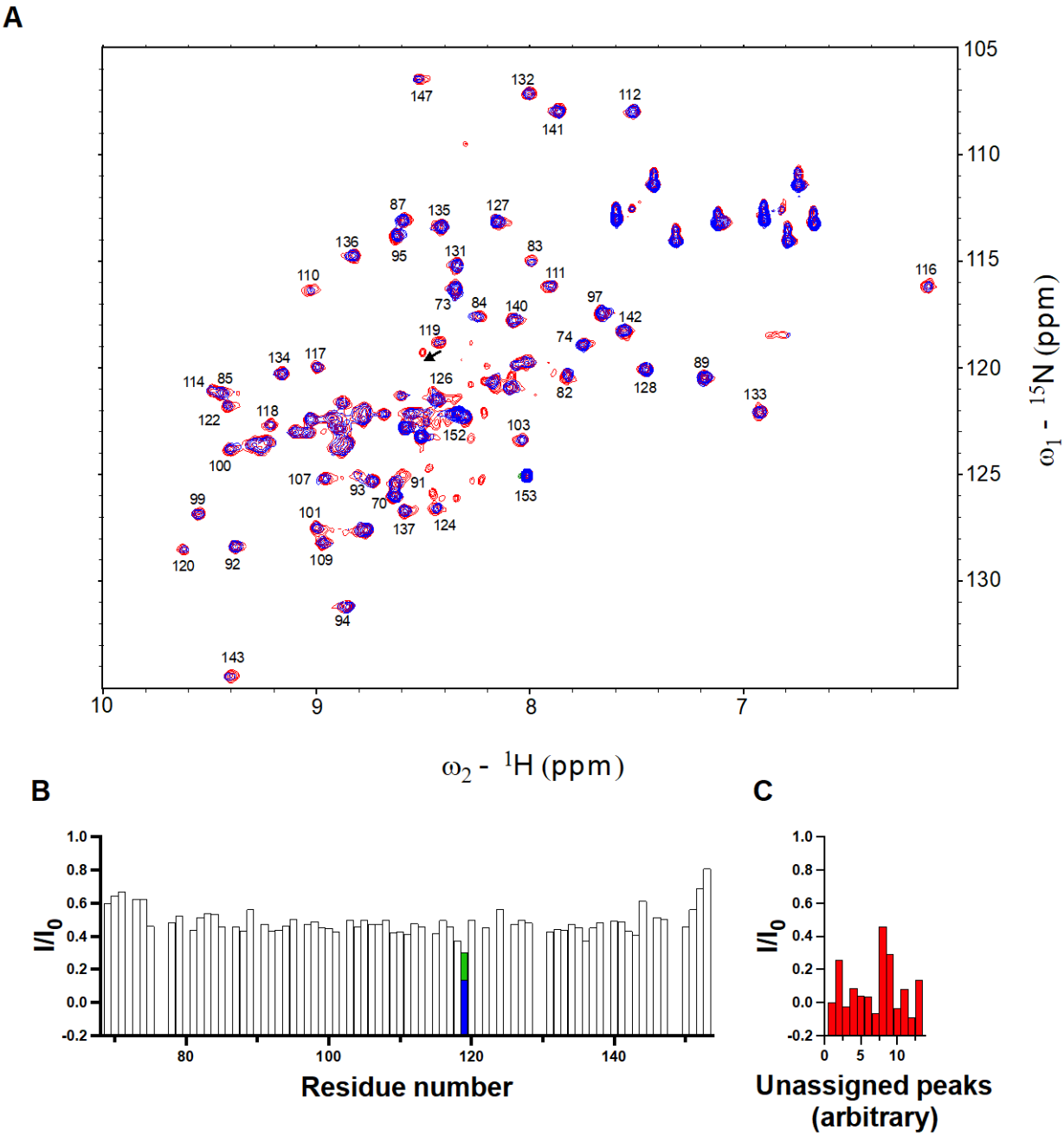
A
105
110
115
120
125
130
ω_1 - ^{15}N (ppm)
10
9
8
7
ω_2 - ^{1}H (ppm)
B
I/I$_0$
1.0
0.8
0.6
0.4
0.2
0.0
-0.2
80
100
120
140
Residue number
C
I/I$_0$
0
5
10
Unassigned peaks
(arbitrary)

Figure 6

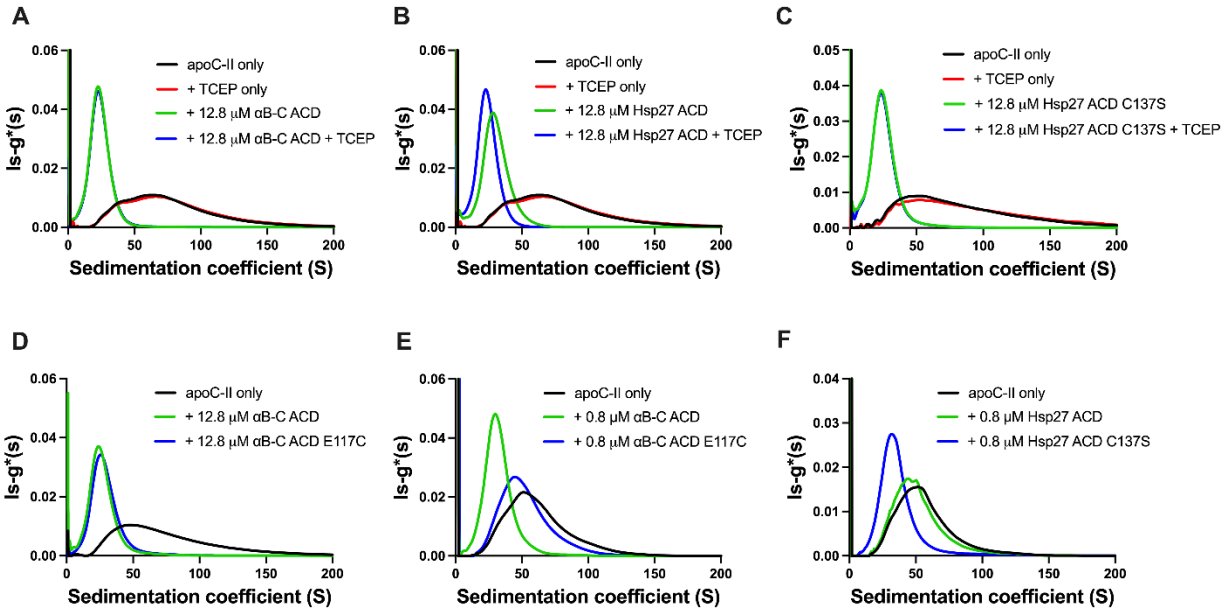
A
apoC-II only
+ TCEP only
+ 12.8 μM αB-C ACD
+ 12.8 μM αB-C ACD + TCEP
ls-g*(s)
Sedimentation coefficient (S)
B
apoC-II only
+ TCEP only
+ 12.8 μM Hsp27 ACD
+ 12.8 μM Hsp27 ACD + TCEP
ls-g*(s)
Sedimentation coefficient (S)
C
apoC-II only
+ TCEP only
+ 12.8 μM Hsp27 ACD C137S
+ 12.8 μM Hsp27 ACD C137S + TCEP
ls-g*(s)
Sedimentation coefficient (S)
D
apoC-II only
+ 12.8 μM αB-C ACD
+ 12.8 μM αB-C ACD E117C
ls-g*(s)
Sedimentation coefficient (S)
E
apoC-II only
+ 0.8 μM αB-C ACD
+ 0.8 μM αB-C ACD E117C
ls-g*(s)
Sedimentation coefficient (S)
F
apoC-II only
+ 0.8 μM Hsp27 ACD
+ 0.8 μM Hsp27 ACD C137S
ls-g*(s)
Sedimentation coefficient (S)

Figure 7

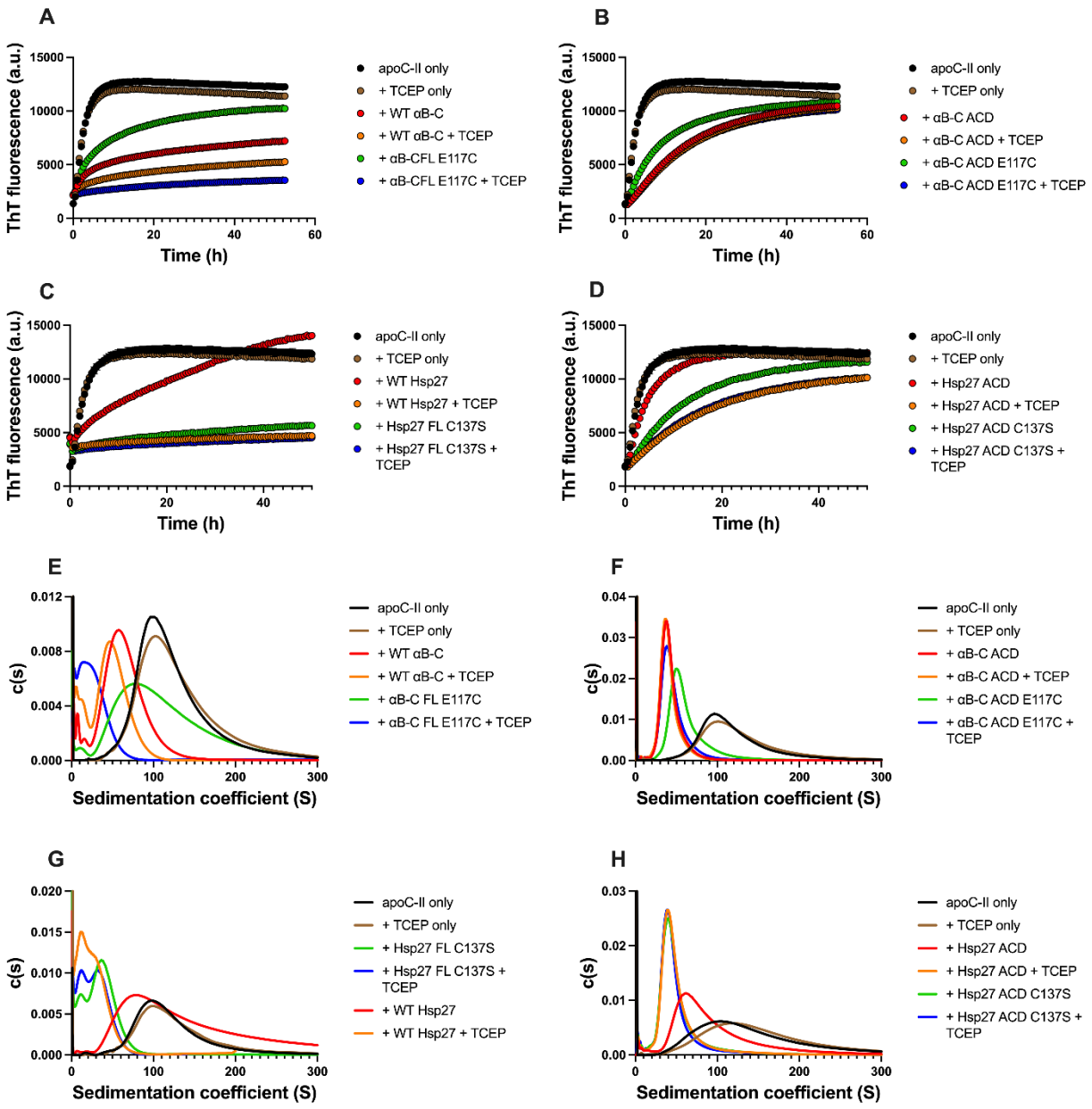
A
ThT fluorescence (a.u.)
Time (h)
apoC-II only
+ TCEP only
+ WT αB-C
+ WT αB-C + TCEP
+ αB-CFL E117C
+ αB-CFL E117C + TCEP
B
ThT fluorescence (a.u.)
Time (h)
apoC-II only
+ TCEP only
+ αB-C ACD
+ αB-C ACD + TCEP
+ αB-C ACD E117C
+ αB-C ACD E117C + TCEP
C
ThT fluorescence (a.u.)
Time (h)
apoC-II only
+ TCEP only
+ WT Hsp27
+ WT Hsp27 + TCEP
+ Hsp27 FL C137S
+ Hsp27 FL C137S + TCEP
D
ThT fluorescence (a.u.)
Time (h)
apoC-II only
+ TCEP only
+ Hsp27 ACD
+ Hsp27 ACD + TCEP
+ Hsp27 ACD C137S
+ Hsp27 ACD C137S + TCEP
E
c(s)
Sedimentation coefficient (S)
apoC-II only
+ TCEP only
+ WT αB-C
+ WT αB-C + TCEP
+ αB-C FL E117C
+ αB-C FL E117C + TCEP
F
c(s)
Sedimentation coefficient (S)
apoC-II only
+ TCEP only
+ αB-C ACD
+ αB-C ACD + TCEP
+ αB-C ACD E117C
+ αB-C ACD E117C + TCEP
G
c(s)
Sedimentation coefficient (S)
apoC-II only
+ TCEP only
+ Hsp27 FL C137S
+ Hsp27 FL C137S + TCEP
+ WT Hsp27
+ WT Hsp27 + TCEP
H
c(s)
Sedimentation coefficient (S)
apoC-II only
+ TCEP only
+ Hsp27 ACD
+ Hsp27 ACD + TCEP
+ Hsp27 ACD C137S
+ Hsp27 ACD C137S + TCEP

Figure 8